Engineering of protein-based phononic crystals for contrast-enhanced ultrasound imaging

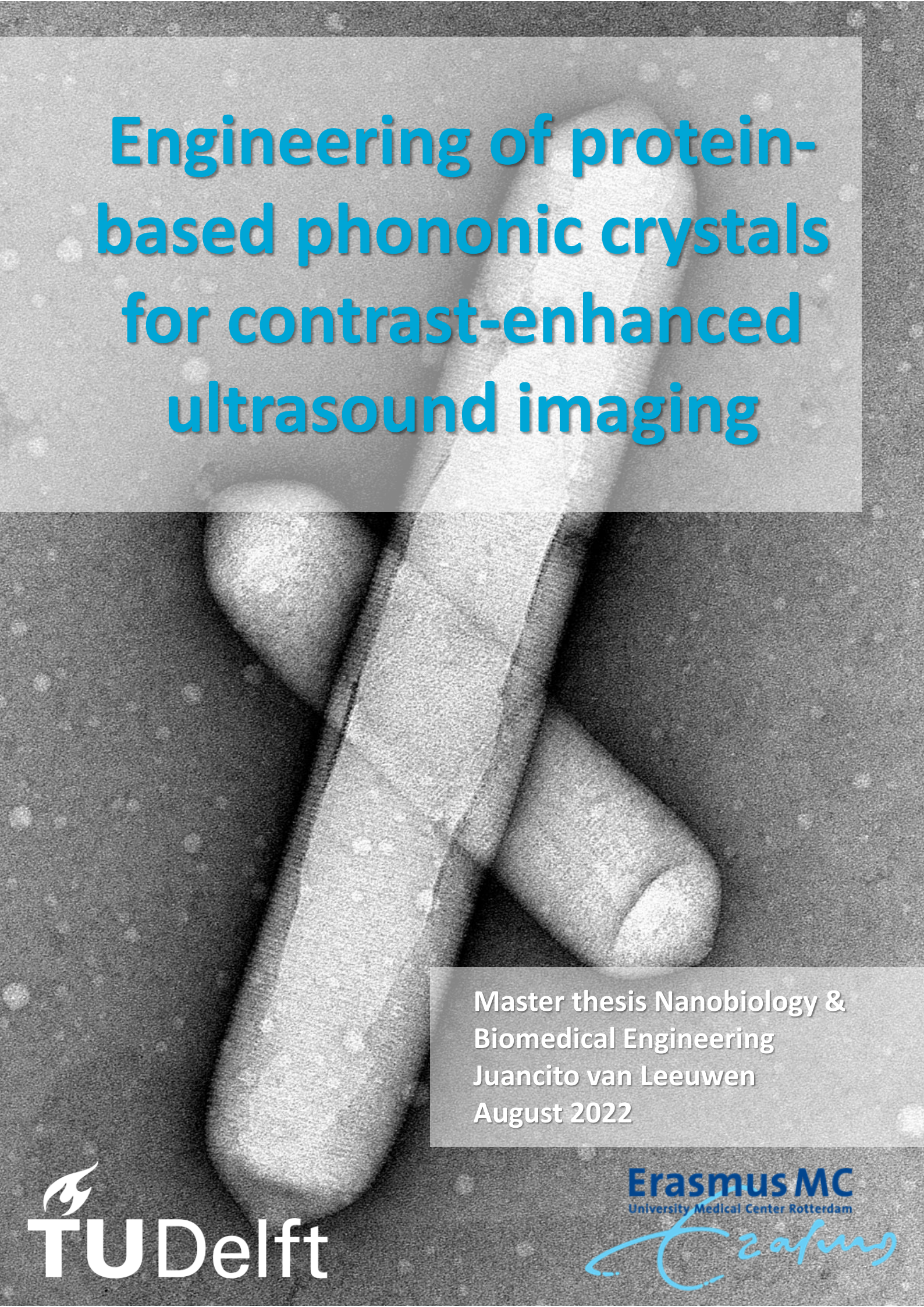

Master thesis Nanobiology & Biomedical Engineering

Juancito van Leeuwen

August 2022

TU Delft

Erasmus MC
University Medical Center Rotterdam

ENGINEERING OF PROTEIN-BASED PHONONIC CRYSTALS FOR CONTRAST-ENHANCED ULTRASOUND IMAGING

A thesis submitted to the Delft University of Technology and Erasmus Medical Center Rotterdam in partial fulfillment of the requirements for the degree of

Master of Science in Nanobiology and
Master of Science in Biomedical Engineering

by

Juancito van Leeuwen

August 2022

Juancito van Leeuwen: *Engineering of protein-based phononic crystals for contrast-enhanced ultrasound imaging* (2022)

The work in this thesis was made in the Maresca and Garbin labs in the following departments:

Imaging Physics and
Chemical Engineering
Faculty of Applied Sciences
Delft University of Technology

Supervisors & examiners:	Dr. David Maresca
	Dr. Valeria Garbin
Examiners:	Dr. Marie-Eve Aubin-Tam
	Dr. Bernd Rieger
Daily supervisor:	Dion Terwiel, Ir.

PREFACE

This thesis is comprised of multiple chapters that describe in detail the periodic aggregation of gas vesicles into phononic crystals and the high-throughput fabrication of encapsulated gas vesicles in alginate beads using microfluidics.

The first chapter contains a general introduction to ultrasound imaging, gas vesicles and microfluidics. Here, I introduce the main concepts of my thesis in more detail, including the main goal: fabricating novel, gas-vesicle-based ultrasound contrast agents. The second chapter is the main body of the thesis, the manuscript. It is written in an IEEE article format to concisely explain the main research findings of my master's end project. In the third and final chapter I discuss the results of the manuscript in more detail, recommend future experiments and provide an outlook on the future applications of these gas-vesicle-based contrast agents. Finally, the appendix contains some additional experiments that were performed that do not necessarily contribute to the final results and conclusions of this thesis but provide useful insights for future work.

Juancito van Leeuwen
Delft, August 2022

ABSTRACT

Contrast-enhanced ultrasound (CEUS) imaging is one of the most widely used biomedical imaging modalities in clinical practice due to its high spatiotemporal resolution and non-invasiveness. However, CEUS imaging techniques rely heavily on microbubble contrast agents that add significant random fluctuations to ultrasound signals and have a limited imaging time. Gas vesicles (GVs), a unique class of stable, air-filled protein nanostructures, have recently been introduced as genetically encoded acoustic contrast agents. While being capable of withstanding higher acoustic pressures and providing smoother hemodynamic ultrasound signals than microbubbles, GVs show a lower ultrasound signal enhancement than microbubbles and are taken up by the liver. The only known solution to enhance ultrasound scattering by GVs, or GV echogenicity, is through GV aggregation. Specifically, periodic aggregation could theoretically maximize contrast since phononic crystals, periodic configurations of air-filled inclusions, are known to significantly amplify sound wave reflections at specific frequencies. Meanwhile, many strategies currently exist in biomedical research to improve biocompatibility. Most interesting is the microfluidic encapsulation in alginate beads, as alginate hydrogels significantly prolong the circulation time of encapsulates while microfluidics offers a high-throughput fabrication method with great control and reproducibility.

In this thesis, a first step is presented towards novel GV-based ultrasound contrast agents with enhanced echogenicity and prolonged circulation times. Using a high-throughput microfluidic approach, periodically aggregated GVs are encapsulated in alginate hydrogel beads.

In order to obtain these novel GV-based ultrasound contrast agents, the contrast enhancement of several GV aggregation strategies, including depletion interactions, fusion proteins and ionic screening, was first investigated. A four-fold increase in nonlinear ultrasound contrast was found for alginate-induced periodic GV aggregation, compared to a two-fold increase for randomly aggregated GVs. This contrast enhancement was found to arise at a concentration of 1.25 mg/ml of alginate. Moreover, a high-throughput droplet-based microfluidic approach was used to encapsulate GVs in $\sim$245 micron beads at a rate of 600 beads per second. Phase contrast microscopy demonstrated the successful encapsulation of GVs, while empty and GV-filled alginate beads both appeared in ultrasound imaging, likely due to entrapped air.

In future work, more advanced microfluidic encapsulation can be explored to fabricate smaller, micron-scale alginate beads without unwanted air-filled cavities. Once successful, and prolonged circulation times have been proven in animal studies, these novel ultrasound contrast agents with improved properties can become the go-to contrast agents for various CEUS applications, including transcranial functional ultrasound imaging.

ACKNOWLEDGEMENTS

First and foremost, I would like to thank my two supervisors, David Maresca and Valeria Garbin. David, thank you for your hospitality and for giving me the opportunity to work in your lab on this exciting intersection between bioengineering and ultrasound. Your open-door policy allowed for many fruitful discussions. Valeria, thank you for your help during our brainstorm sessions as well as all of the hard work you did for me behind the scenes. I would also like to thank Marie-Eve Aubin-Tam and Bernd Rieger for being members of my assessment committee. To past and present Maresca and Garbin lab members, and students in the Medical Imaging student room: I could not have done this without you. Specifically, Dion Terwiel, my daily supervisor, who has helped me from the start but also showed a lot of trust and let me do things on my own. Thank you! Baptiste Heiles, thank you for many interesting insights and discussions on ultrasound during (and after) our lab meetings. Rick Waasdorp and Olivia Weidlich, your help with imaging and MATLAB was most definitely appreciated (and needed). Tara, I am grateful for all of your hard work in preparing the countless number of GVs I used during my project. I would like to thank Stefan Huber for his help with TEM imaging and especially his excitement about GVs. Thank you to Margherita Tavasso, Zaid Rahman and Kristen David for their much needed help in the microfluidics lab, as well as to Daan Brinks, Arjen Jakobi and Pouyan Boukany for allowing me to use their labs and facilities. I would also like to thank my friends and family for their unwavering support and pretending to understand what I was talking about when I explained what my research was about. My parents, ever far on the sunny Bonaire but always on my mind and in my heart, thank you as well. And finally, a special thanks to Iris Bakker, who helped me through more than a few stressful moments with kindness and grace.

...

CONTENTS

ACRONYMS

1 INTRODUCTION

Already in the 17th century, Robert Hooke predicted that in the future, humans would be able to image the human body with sound. In "The Posthumous Works of Robert Hooke", Hooke speculates that sounds may contain specific information about the conditions of their source in an "acoustic code" [1, 2]. He recognized that barely audible vibrations contain just as much information as those that are easily heard, and conjectured that if these vibrations were made more accessible, through amplification, for example, analyzing them could reveal the nature and functioning of otherwise concealed internal activities. While the stethoscope would not be invented for another century, he clearly already anticipated its discovery. However, it was not until the 1940's that the first ultrasound scan of the human body would be made [3].

Today, ultrasound is among the most widely used biomedical imaging modalities in clinical practice. It is used daily to assess organ anatomy and physiology, has diagnostic purposes in obstetrics and cardiology, and there is a growing interest from the field of neuroscience [4, 5]. With the use of synthetic ultrasound contrast agents, contrast-enhanced ultrasound imaging has revolutionized the field of ultrasound imaging, and has improved the diagnostic performance in numerous pathological conditions [6]. More recently, a new class of hemodynamic enhancers based on gas vesicles was introduced for ultrasound imaging [7]. They have shown that gas vesicles can withstand higher ultrasound pressures and introduce less signal fluctuations than clinically used microbubble contrast agents [8]. Moreover, the genetic encodability and biochemical composition of gas vesicles allow for a wide range of applications, ranging from the detection of enzyme activity to cell-specific molecular targeting [9–11]. Unfortunately, limitations of these techniques include a relatively lower echogenicity compared to microbubbles and a limited circulation time in the blood stream of tens of minutes [8, 12].

Therefore, the main goal of this work is to fabricate a novel, gas vesicle-based contrast agent with maximized ultrasound contrast and a prolonged circulation time. In order to achieve this, a droplet-based microfluidic approach is explored, as it enables reliable and reproducible high-throughput fabrication of monodisperse droplets as isolated sample containers. To tackle the limited echogenicity, the periodic aggregation of gas vesicles into protein-based phononic crystals is explored.

1.1 ULTRASOUND IMAGING

As one of the most widespread clinical imaging modalities, ultrasound is used in diagnostics, surgery guidance and therapy in many different medical fields [3]. Conventional ultrasound images are of thin, flat sections of the body, while more advanced ultrasound technologies allow for volumetric, 3-D images [13]. Doppler ultrasound is a special ultrasound technique that is capable of evaluating the movement of materials in the body, such as blood flow through arteries and veins [14]. Ultrasound imaging is free of radiation risk, making it safe and noninvasive, and is relatively inexpensive when compared to magnetic resonance imaging (MRI), computed tomography (CT) and nuclear imaging. Furthermore, it is portable and easy to use, since the machines are small and flexible. The main advantage, however, is that

ultrasound has a high spatiotemporal resolution (down to 100 µm and 10 ms), providing real-time, high-resolution images [15, 16].

Ultrasound imaging makes use of acoustic waves, which are pressure disturbances propagating through a compressible medium at a medium dependent speed of sound. In medical ultrasound, the propagation of longitudinal pressure waves induces particle displacement parallel to the direction of wave propagation. A pressure wave is characterized by its frequency (f), velocity (c = speed of sound) and wavelength (λ) by: $\lambda = c/f$. The term ultrasound stands for any sound waves with a frequency above 20 kHz, but medical ultrasound makes use of frequencies in the megahertz range (1–15 MHz) [3].

An ultrasound signal is obtained using an ultrasound transducer or probe, which consists of an array of piezo-electric elements. These elements are capable of transmitting and receiving short ultrasound pulses at a given central frequency by transforming an electrical signal into a pressure displacement and vice versa. Once transmitted, acoustic waves propagate deep within the body with a certain speed of sound, which for soft tissue at 37 °C is on average 1540 m/s [17]. When an acoustic wave encounters a planar interface between two different tissues, part of the wave is transmitted and part is reflected back towards the transducer, as shown in Figure 1.1a. The fraction that is reflected is called the reflection coefficient (R), and is determined by:

$$R = \frac{A_r}{A_i} = \frac{Z_2 - Z_1}{Z_2 + Z_1}. \tag{1.1}$$

Here, A_i and A_r are the amplitudes of the incident and reflected pressure waves, and Z_1 and Z_2 are the acoustic impedances of tissues 1 and 2, respectively [18]. The acoustic impedance of a medium depends on the density (ρ) of the medium and the speed of sound (c) of a pressure wave propagating in that medium: $Z = \rho c$.

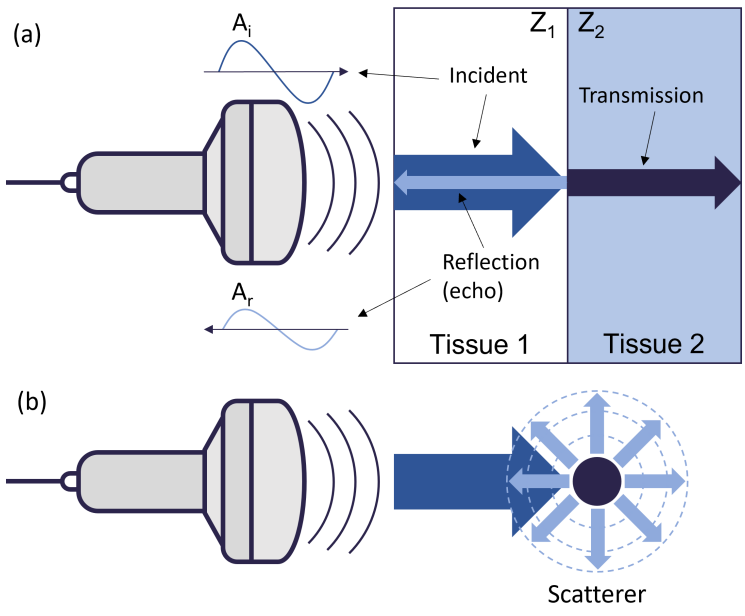

Figure 1.1: Ultrasound wave reflection and scattering. (a) Reflection and transmission of an acoustic wave at a planar interface between two tissues with different acoustic impedances. (b) Spherical scattering of an acoustic wave by a Rayleigh scatterer.

It is these interactions between ultrasound and tissues that enable the detection of organ contours and assessing organ anatomy. The depth of tissue interfaces where reflections take place can be estimated by measuring the time it takes for the acoustic waves to travel from the source to the interface and back. Since the speed of

sound in the medium is known (~1540 m/s), the distance to the reflective interface is proportional to the traveling time. The relative change in the amplitude of the pressure wave between transmitting and receiving provides information about the tissues at the interface. If the change in amplitude is low (small R), only a small portion of the incident wave will have been reflected, meaning the acoustic impedances of the two tissues are similar. However, if the impedance mismatch is large, R will be close to 1, meaning almost the entire wave will have been reflected. Air, for example, has a low acoustic impedance, while dense and compact organs have the highest acoustic impedance. Bone and air-filled structures such as the lungs therefore create poor acoustic windows for ultrasound transmission, as most of the energy gets reflected due to high impedance mismatch [19].

When an ultrasound wave impinges on reflectors whose dimensions are smaller than the wavelength of the incident wave, such as red blood cells or subcellular structures, an echo is scattered in all directions in the form of a spherical wavefront (Figure 1.1b) [19]. The reflective power of a so-called *Rayleigh point scatterer* is defined by the scattering cross-section:

$$\sigma_S \propto V_S^2 f_U^4 \left(\left(\frac{\kappa_S - \kappa_0}{\kappa_0} \right)^2 + 3 \left(\frac{\rho_S - \rho_0}{2\rho_S + \rho_0} \right)^2 \right). \tag{1.2}$$

Here, V_S is the volume of the point scatterer and f_U is the ultrasound frequency [5]. Compressibility constants κ_S and κ_0, and densities ρ_S and ρ_0 are properties of the point scatterer and its surrounding medium, respectively. It is clear from Equation 1.2 that if a particle does not exhibit a significant difference in compressibility and/or density compared to the surrounding medium, it will scatter ultrasound waves weakly. This is the case for red blood cells in the surrounding aqueous blood plasma, for example, and blood vessels will therefore often appear dark in conventional ultrasound imaging techniques.

However, imaging of blood vessels and blood flow is of great importance in medicine. Many diseases are diagnosed based on vasculature and blood flow, such as different types of cancer, cardiovascular diseases and neurological disorders [20–23]. Imaging blood vessels can also aid in treatment planning and surgical procedures [24, 25]. While MRI is capable of imaging blood and blood flow dynamics, the ease-of-use and low cost of ultrasound imaging make it a more attractive imaging technique in clinical practice. Furthermore, the portability of ultrasound systems allows for bed-side imaging as well as use inside the operating room. Therefore, it is important to enhance the available contrast of the blood in an ultrasound image. Fortunately, there are various imaging techniques such as Doppler ultrasound imaging that are capable of visualizing blood flow via ultrasound. Additionally, clinicians are able to enhance the echogenicity (the ability to backscatter ultrasound signals efficiently) of blood in ultrasound using injectable ultrasound contrast agents (UCA), in what is called contrast-enhanced ultrasound (CEUS) imaging [26].

1.2 CONTRAST-ENHANCED ULTRASOUND IMAGING

CEUS was a major breakthrough in ultrasound imaging. By using UCAs and contrast-specific imaging techniques, CEUS is able to depict blood micro- and macrocirculation, which leads to an improved performance in many diagnoses [27]. In echocardiography, for example, improved contrast allows for better assessment of cardiac structure and function, and assists in the detection and classification of intracardiac masses [6]. CEUS is particularly suitable for liver imaging, due to the liver's special dual blood supply system. By looking at the behavior of UCAs in the vessels inside and surrounding the liver, it is possible to determine whether liver lesions are malignant or not [27]. More recently, using UCAs and a technique called ul-

trasound localization microscopy, scientists have even been able to map the neural vasculature in rats and humans with super-resolution accuracy (Figure 1.2a) [28,29]. Another technique that has seen recent advancements through UCAs is functional ultrasound (fUS). fUS is a breakthrough technology that maps neural-activity-induced changes in local cerebral blood volume, by correlating neural stimulation with ultrasound power Doppler signal from the brain (Figure 1.2b&c) [30]. By artificially enhancing the available contrast in the cerebral vasculature, UCAs significantly improve the specificity and resolution of fUS, and prevent the need for invasive surgical procedures such as craniotomies or thinned-skull preparations [8, 31].

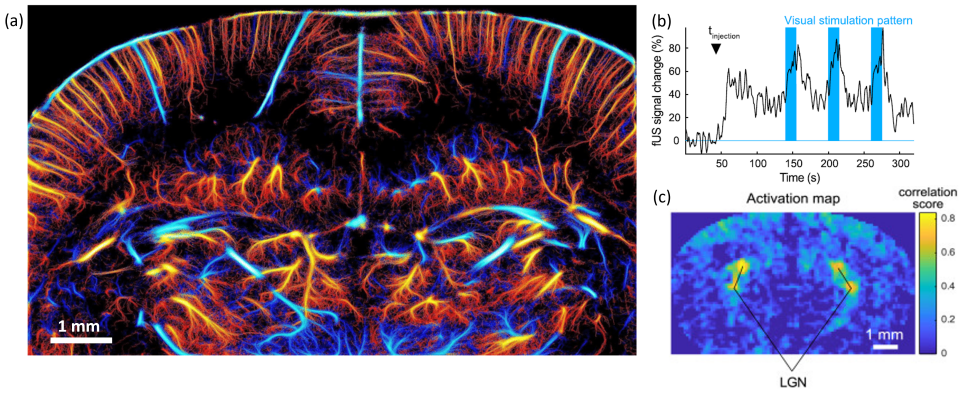

Figure 1.2: Two ultrasound contrast agent applications. (a) Ultrasound localization microscopy image of the rat brain vasculature (from Couture et al. 2018 [28]). (b) Visual stimulation pattern (blue) overlaid on UCA-enhanced fUS signal of the lateral geniculate nuclei (LGN) in the mouse brain and (c) the resulting fUS neural activation map of the mouse brain showing activation of the LGN in response to visual stimulation (from Maresca et al. 2020 [8]).

1.2.1 Synthetic contrast agents

The only clinically available class of UCAs are lipid-shelled microbubbles (MB). MBs have large differences in their compressibility and density (i.e. acoustic impedance) compared to their surrounding aqueous medium, and can thereby significantly enhance the amount of scattering in the blood stream (following Equation 1.2). MBs can also exhibit resonance, and as a consequence they can enhance scattered ultrasound signals up to 30 decibels (dB) compared to red blood cells [32]. MBs are composed of an inner core of trapped gas (usually heavy, non-water-soluble gases like perfluorocarbon) encapsulated by an extremely thin shell consisting of lipids, albumin or other surfactants. This thin shell also provides the flexibility needed for the MB's acoustic response. Due to their compressibility, MBs undergo radial oscillations when insonified by an oscillating pressure wave, which in turn gives rise to a secondary sound wave [33]. This secondary sound wave is highly nonlinear, meaning the frequency response of this wave contains higher harmonic frequencies of the initial, fundamental frequency that was used to insonify the MBs. In the last few decades, ultrasound imaging techniques have been developed that are capable of separating this nonlinear MB response from the more linear anatomical background, which will be discussed in a later paragraph (subsection 1.2.3).

Unfortunately, the use of MBs also has limitations. Because of the trapped gas core, a partial pressure gradient arises between the MB's interior and the outside, which is inversely proportional to its radius [34]. This is what limits MBs to sizes larger than 1 µm, and also leads to gas escape, bubble fragmentation and ultimately, MB collapse. All of these factors lead to a short halflife compared to the *in vivo* dynamics of cancer, immune or stem cells, and limit the imaging window to several minutes. Additionally, it has been shown that MBs introduce many fluctuations in

received ultrasound signal [8]. This is especially limiting in the case of fUS, where any small variation could distort the correlation with neural activation and thereby provide an inaccurate activation map.

No other contrast agents proposed as MB alternatives have so far been widely adopted, due to limitations in e.g. stability or echogenicity. While further research into optimization of MB properties is an active field of research, scientists have recently identified a new type of acoustic biomolecule for ultrasound imaging, namely bacterial nanostructures in the form of gas vesicles (GV) [7].

1.2.2 Genetically encoded contrast agents

GVs are genetically encoded gas-filled protein nanostructures with widths of 45–250 nm and lengths 100–600 nm, depending on the species of origin [7,35]. They are expressed intracellularly in certain photosynthetic microbes to help modulate cellular buoyancy in an aqueous environment for optimal access to nutrients and light (Figure 1.3a). To provide a cell with buoyancy, many GVs are needed, which are often packed tightly together along their long axis in hexagonal arrays for packing efficiency. GVs comprise a 2 nm thick protein shell in a cylindrical or bi-conical shape, which is hydrophilic on the outside and extremely hydrophobic on the inside. The wall allows gas to freely diffuse in and out of the shell but prevents any liquid from condensing on the inside, creating a stable pocket of air inside the microorganism. It is important to note that this interaction with gases is fundamentally different from that in MBs, which trap pre-loaded gas in an unstable configuration. In the case of GVs, no partial pressure gradient exists between the in- and outside of the shell, making them inherently stable despite their nanometer size. The low density and high compressibility of GVs relative to their surrounding aqueous media gives rise to an acoustic impedance mismatch. This in turn allows the GVs to strongly scatter acoustic waves (Equation 1.2) and thereby produce a strong ultrasound contrast, even at picomolar concentrations [7,9]. GV concentrations are typically measured using optical density (OD) at 500 nm in a spectrophotometer, and OD = 1 corresponds to 114 pM GVs [36].

GVs have been found in over 150 species of prokaryotes [37] (bioRxiv preprint). One of the most well studied in the context of acoustic biomolecules are from *Anabaena flos-aquae* (Ana), a cyanobacterium often found in freshwater ponds and lakes. Ana GVs are encoded by a cluster of 9 genes, which include structural proteins and assembly factors needed for GV formation [35]. The two primary structural proteins are gas vesicle protein A (GvpA) and gas vesicle protein C (GvpC) [38] (bioRxiv preprint). GvpA is a 7.4 kDa protein with both hydrophilic and hydrophobic sidechains that assembles into the main structural shell. GvpA forms ribs that run perpendicular to the long axis of the GV, with its hydrophobic side chains pointing inwards and its hydrophilic sidechains pointing outwards. The nanoscopic space in between subsequent ribs is where gas is able to freely diffuse into and out of the GV. GvpC is a 22.0 kDa protein that is mainly α-helical, and strengthens the GV shell by binding across several GvpA repeats on the exterior surface [35].

The genetic encodability and biochemical composition of GVs make it possible to engineer their physical properties and surface functionalities. For example, it is possible to engineer GvpC to modulate the acoustic and mechanical properties of GVs, including targeting specificity or adding fluorescent labels (Figure 1.3b) [9]. Additionally, it is possible for GVs to produce nonlinear ultrasound signals [39]. Regular wild-type (WT) GVs behave as linear ultrasound scatterers, meaning that they scatter incoming ultrasound waves in all directions with the same frequency content as the initial pulse. Alternatively, "stripped" or harmonic gas vesicles (hGV) can be obtained by stripping GvpC from the outer shell through biochemical reactions, or through truncations in its DNA sequence. These hGVs have weaker shells and are more flexible than native WT GVs, making them susceptible to deformations ("buckling") at lower acoustic pressures. While this weakening of the shell lowers the

pressure at which they collapse, the buckling that occurs when insonifying hGVs with ultrasound pressure waves above the buckling threshold is what causes the incoming wave to scatter with higher harmonics and thus produces nonlinear contrast (Figure 1.3c). A similar effect occurs when insonifying MBs at specific pressures, which will start to oscillate radially and also generate nonlinear signals [33].

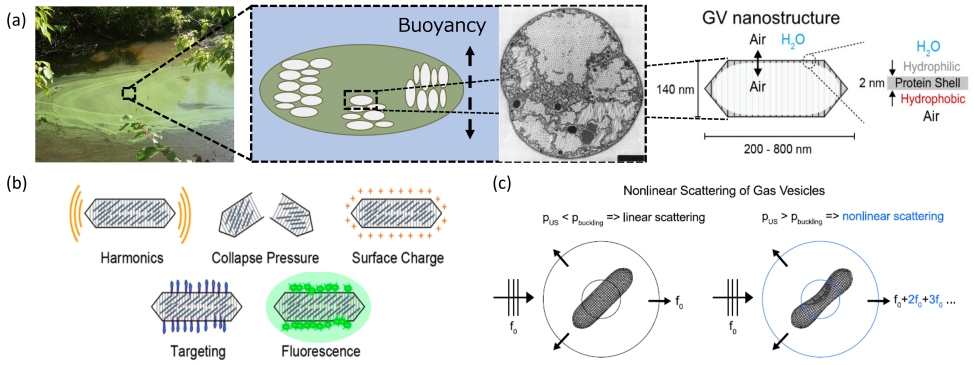

Figure 1.3: Gas vesicle origin and properties. (a) GVs are derived from photosynthetic microbes, often found in sweet water ponds. Thin-section electron micrographs show the packing configuration of GVs inside microbes (from Walsby 1994 [35]). The schematic representation of the GV nanostructure depicts GV dimensions (from Lakshmanan et al. 2016 [9]). (b) GV properties can be modulated through biochemical or genetic GvpC engineering (from Lakshmanan et al. 2016 [9]). (c) hGVs insonified with pressures below the buckling threshold exhibit linear scattering, while hGVs insonified with pressure above the buckling threshold will buckle and therefore exhibit nonlinear scattering (from Maresca et al. 2018 [40]).

1.2.3 Ultrasound contrast agent imaging modalities

Several different ultrasound imaging techniques exist capable of visualizing UCAs. Conventional 2D ultrasound images are created by repeatedly transmitting a thin, focused beam of acoustic waves into the tissue and receiving the echoes. The amplitude of each echo is detected and converted into pixel intensities in a process called "beamforming". The most widespread beamforming technique, delay-and-sum, introduces specific time delays to the received echo signals of each transducer element so that they can be summed constructively in the desired receive directions, while attenuating the signals from undesired directions [41]. The calculated delays are geometrically determined (the greater the receive angle, the greater the delay) and depend on the assumed homogeneous speed-of-sound in the tissue. However, the downside of line-by-line imaging is that image acquisition is slow, with image rates on the order of tens of frames per second.

Significant technological advances in the past decades have enabled ultrasound imaging and image reconstruction at much higher frame-rates. In plane wave imaging, for example, all array elements transmit a pulse simultaneously, creating a planar wavefront. Final images are obtained using similar beamforming techniques such as delay-and-sum. Since only a single plane wave transmission is needed to insonify the entire imaging plane, plane wave imaging can be as much as two orders of magnitude faster than conventional line-by-line imaging [16].

Line-by-line and plane wave imaging sequences are more commonly known as B-mode imaging, where the pixel intensities are determined by the amplitudes of the returned echo signal. Special ultrasound techniques also exist that make use of a combination of pulse sequences. Doppler imaging is used to look at blood flow through high-frame rate imaging, by sending and receiving many plane waves in a short period of time. By looking at the relative temporal shift of consecutive

echoes in subsequent frames, Doppler imaging is capable of retrieving the velocity of moving particles (like red blood cells and UCAs) inside the body [42].

These sequences typically show linear reflections, i.e. the frequency content of the received signal is similar to that of the transmitted ultrasound pulse. However, certain ultrasound pulse sequences have been developed that depict only nonlinear scattering, thereby improving the contrast of nonlinear UCAs with linear anatomical background. Amplitude modulation, for example, can detect differences in backscattered ultrasound frequencies by subtracting the obtained signal of a transmission with full amplitude by two subsequent transmissions with half amplitude (Figure 1.4a). A half amplitude transmission can be achieved by silencing odd or even elements of the transducers, while a full transmission makes use of the entire array. Any linear behavior will be cancelled out, whereas the nonlinear signal that arises from the high pressures in the full amplitude case will remain [39]. Nonlinear imaging modes are capable of distinguishing nonlinear hGVs from anatomical background or linear WT GVs (Figure 1.4b).

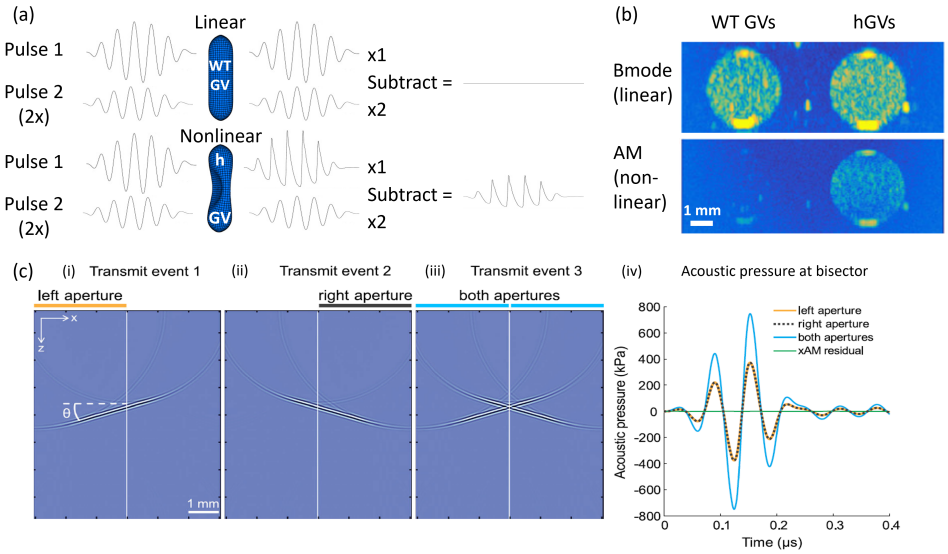

Figure 1.4: Nonlinear ultrasound imaging of gas vesicles. (a) Principle of amplitude modulation. Amplitude modulation cancels out echoes from linear scatterers and anatomical background, but not from nonlinear scatterers (GV illustrations from Maresca et al 2017 [39]). (b) Nonlinear ultrasound imaging shows only hGVs, while regular linear B-mode imaging shows both WT and hGVs (modified from Maresca et al. [39]). (c) Principal of crosswave amplitude modulation (xAM) ultrasound imaging. Two angled half aperture transmit events (i & ii), followed by a full aperture transmit event (iii) lead to a reduced time of the residual wavefront spent at high amplitudes (iv) (from Maresca et al. 2018 [40]).

Unfortunately, the specificity of nonlinear ultrasound imaging techniques is compromised by nonlinearity added by UCAs to the propagating waves, due to pressure-dependent attenuation of ultrasound waves [3, 43, 44]. Consequently, the frequency band will be contaminated, resulting in strong imaging artifacts downstream of the UCAs. To resolve this, xAM imaging was developed to efficiently reduce nonlinear propagation artifacts by minimizing the area insonified by higher amplitude pressure waves (Figure 1.4c) [40]. It consists of three consecutive ultrasound transmission events. The first two transmissions are plane waves transmitted at a specific angle using only the left and right half of the transducer, respectively. The third transmission is a combination of the previous two, creating a cross-propagating, or "X", wave. Only at the intersection of this propagating "X" will the amplitude be double that of the rest of the wave, thereby minimizing the time of the wave front

spent at double amplitude (see green line in Figure 1.4c.iv). This has been shown to effectively reduce nonlinear wave propagation and related artifacts.

In recent studies, functionalized GVs have been introduced as acoustic biosensors that "light up" in such nonlinear imaging modes, as a response to certain enzymatic activities that weaken their shells [11]. These studies provide a handle to engineer acoustic biosensors with tuneable nonlinear contrast. Unfortunately, GVs also have limitations. While being inherently more stable than conventional MBs, it has been shown that GVs have a limited circulation time in the blood stream of tens of minutes due to the host body's immune response [12]. Moreover, due to their nanoscopic size and lower gas fraction, GVs show a reduced echogenicity in comparison to MBs [8].

To maximise the potential of this nanotechnology, a diversification of GV acoustic properties is necessary. Enhanced GV scattering would facilitate their detection deep within tissues while diverse nonlinear responses would enable the imaging of different targets simultaneously.

1.2.4 Gas vesicle aggregation

One proposed solution to enhance the scattering of ultrasound waves by GVs is through GV aggregation [7, 45]. By attaching biotin markers to the outside surface of GVs and introducing the right amount of streptavidin molecules, it is possible to aggregate GVs in random configurations (Figure 1.5a). It has been shown that such aggregation can improve ultrasound contrast by several dB [7]. However, introducing too much streptavidin will oversaturate the biotin markers, thereby preventing aggregation and any contrast enhancement.

It is known that, through complex interactions involving multiple scattering reflections, nonlinear wave propagation and resonance, phononic crystals of air-filled inclusions are able to strongly attenuate or enhance acoustic waves in specific frequency bands [46–48]. Phononic crystals are typically composed of periodic inclusions, or scatterers, in a matrix. They are designed to control the dispersion of acoustic waves with wavelengths comparable to the dimensions and periods of the scatterers. Therefore, it is hypothesized that by aggregating GVs into such periodic configurations, the produced ultrasound contrast could be maximized. Through multiple reflections in periodic GV assemblies, the mean free paths of ultrasound waves are significantly longer, which likely causes a build up of signal nonlinearities. In nature, GVs are in fact compacted into periodic arrangements inside compartments of microbes, to maximize packing efficiency [35]. Recently, periodic GV aggregation has been replicated in a laboratory setting with the help of so-called depletion interactions [49].

Depletion interactions are the effective attractive force that arises between impermeable particles when suspended in a concentrated solution of solutes that are preferentially excluded from the vicinity of these particles, i.e. depletants [50]. By packing the particles close together, the gaps (or "excluded volume") between them are eliminated, thereby creating more free space for the depletants to diffuse. Since the concentration of depletants substantially exceeds that of the suspended particles, creating more space for the depletants maximizes the translational entropy, as there are more configurations for the system to be in. This creates the thermodynamic driving force that packs the particles together. Since GVs are cylindrical in shape, the packing configuration that minimizes the gaps between them is along the long axes (Figure 1.5b) [51].

It has already been seen using transmission electron microscopy (TEM) that periodic GV aggregation is possible using a concentrated enough solution of dextran, a long, branched polysaccharide (Figure 1.5c) [49]. In the same study, it was shown that by suspending GVs in a solution of electrolytes, GVs tend to aggregate in a semi-random configuration (Figure 1.5d). This is due to the masking of the net negative charge of the GV's outer surface by the positive ions. By removing this

repulsive force among GVs, Van der Waals interactions, a generic attractive force acting on two objects, will cause GVs to pack together. Naturally, other molecules could achieve the same types of GV interactions. Polylysine, a genetically encodable multivalent polypeptide with positive charges, has the same effect as electrolytes, while negatively charged DNA has a similar effect as dextran. Another well-known depletant that is hypothesized to work, is alginate.

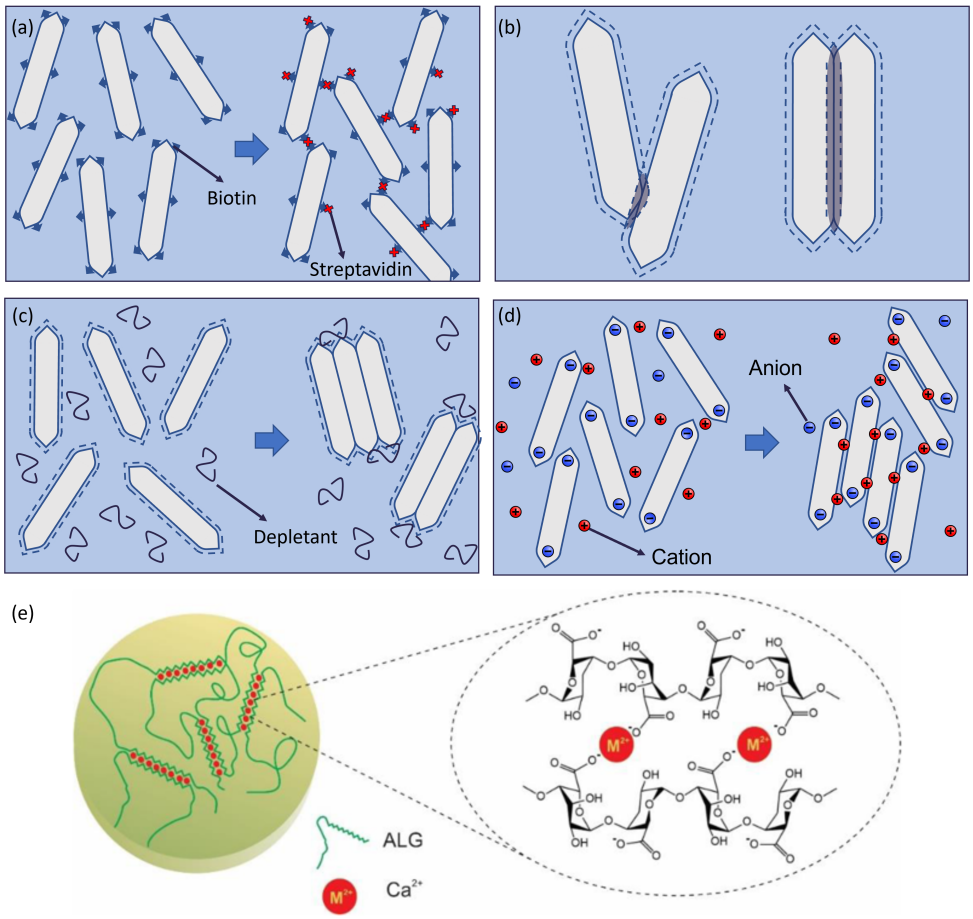

Figure 1.5: Gas vesicle aggregation strategies and alginate gelation. (a) Aggregation of biotinylated GVs using streptavidin. (b) Aggregation of rod-like particles along their long axis maximizes the overlap of exclusion volumes. (c) Periodic GV aggregation through addition of depletants. (d) GV aggregation through addition of electrolytes. (e) Calcium ions cross-link alginate polymers and induces gelation (from Hu and Lo 2021 [52]).

Alginate is a naturally occurring linear polysaccharide polymer obtained from brown seaweed algae. It has been extensively investigated and is used for many applications in pharmaceutical, cosmetic, biomedical and food industries, due to its biocompatibility, biodegradability, low toxicity and low cost [53]. In 1938 it was observed that, upon addition of alginate molecules, a solution of rubber latex started to rapidly coagulate, making it one of the first reports of depletion interactions [54]. Additionally, one of the most interesting characteristics of alginate is its ability to form a hydrogel when it comes in contact with multivalent cations such as Ca^{2+}. Calcium ions act as cross-linkers between the structural units of alginate chains (Figure 1.5e). Although various multivalent cations can be used for gelation, calcium ions are most frequently used since they are clinically safe, readily available and cheap. The gelation process occurs under mild conditions, providing an ideal environment for e.g. drug or cell encapsulation, since no external forces are applied to damage the encapsulated objects. Due to these many advantages, alginate is often

used in the pharmaceutical industry for drug or protein delivery. Alginate encapsulation of small drugs significantly enhances the biocompatibility and circulation time, and allows for controlled release of drugs through the nanoscopic pores of the hydrogel [53].

Conventional techniques used to fabricate alginate-hydrogel microparticles include inkjet printing, spray drying and membrane emulsification. Unfortunately, the fabricated particles are often polydisperse or too large for *in vivo* applications. Therefore, a lot of research is being done on the fabrication of alginate microparticles using microfluidics [55].

1.3 HIGH-THROUGHPUT DROPLET FABRICATION USING MICROFLUIDICS

Microfluidics is the science of precisely controlling and manipulating fluids confided to sub-millimeter channels. Over the past few decades, microfluidics has found its way into many different biomedical applications, ranging from drug discovery and delivery, to cellular analysis and tissue engineering [56, 57]. The main reason for this shift towards small scale systems is the unparalleled level of control over experimental conditions achievable using microfluidics, such as pressure, concentrations and flow rates. This control is made possible because microscale fluid flow is almost always laminar and thus highly predictable. Another advantage of working at the microscale is that microfluidic systems inherently work with small quantities of samples and reagents, making it efficient and inexpensive. Finally, microfluidics is a flexible and versatile technology. The small size makes it portable, and depending on the channel geometry, there are many ways to manipulate fluids for various applications. One microfluidic geometry that has gained considerable attention is that of droplet generators.

Droplet-based microfluidics relies on the high-throughput production and manipulation of droplets with a controlled size and low dispersity. In microfluidics, a wide variety of techniques are available to generate and manipulate droplets at a great frequency (up to thousands of droplets per second) [58]. The most commonly used techniques are so-called passive droplet generation methods, where monodisperse droplets are generated in nozzles with co-flowing, flow-focusing or T-junction geometries (Figure 1.6) [59, 60]. Of these three, flow-focusing enables a larger flexibility in droplet size tuning and higher generation frequencies [61]. All three of these methods rely on the flow field to deform the interface between two or more phases, i.e. two or more immiscible or partially miscible fluids. The deformation of the liquid-liquid interface will eventually lead to the breakup (or "pinching") of the fluid stream into droplets. The dispersed phase droplets will then flow through the rest of the microfluidic channel in the continuous phase, which is often some type of oil and a surfactant. The droplets can then either be collected immediately, or first be subject to manipulation such as droplet fission, fusion or sorting.

Several fluid and geometry parameters influence the droplet-generating process, such as the viscosities, densities and flow rates of the phases, as well as the width and height of the channels and flow focusing orifice [61]. However, no model exists that reliably predicts the droplet size and generation frequency as a function of device dimensions and flow parameters. Fortunately, many experimental and numerical studies have qualitatively shown the scaling laws that apply. For example, smaller flow focusing orifices and channel geometry allow for smaller droplets [60, 61]. Additionally, if the two "pinching" channels of the continuous phase are at an acute angle rather than perpendicular, smaller droplets can be obtained [62]. It is also known that larger flow rate (Q_{cont}/Q_{disp}), density (ρ_{cont}/ρ_{disp}) and apparent viscosity (μ_{cont}/μ_{disp}) ratios lead to smaller droplets [63]. The spacing of droplets is also very dependent on flow rates. Overall, a higher dispersed

phase flow rate leads to a higher generation frequency and thus a smaller spacing [64]. It must be noted that droplets are only generated for specific combinations of flow parameters, fluid characteristics and geometries. If fluids are too viscous or flow rate ratios too high, the dispersed phase will form a stream inside of the continuous phase, rather than droplets, or could start to flow into the wrong channels (Figure 1.6) [60]. The control of the fluid rates is done by either applying a controlled pressure difference over the device, or by enforcing a flow rate using a syringe pump.

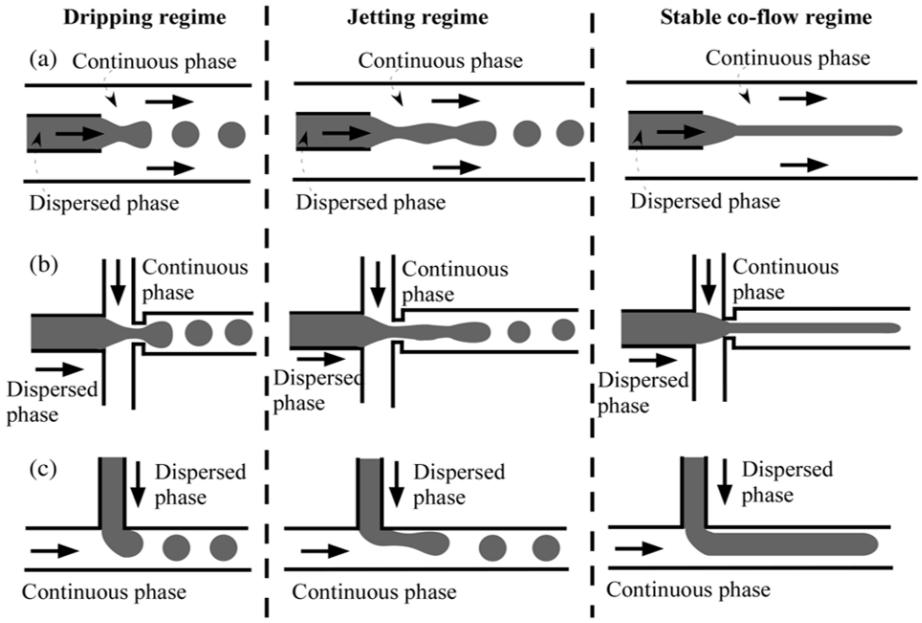

Figure 1.6: Schematic of different flow regimes in droplet-based microfluidics. Dripping (left), jetting (middle) and stable co-flow regimes (right) for (a) co-flowing, (b) flow-focusing and (c) T-junction microfluidic geometries. Solid arrows indicate the flow direction. In the dripping regime, dispersed phase drops detach from the injection source and proceed downstream by the flow of the outer continuous phase. In the jetting regime, the dispersed fluid can flow out of the source as a single thread or "jet", and droplets pinch off from the tip. In the stable co-flow regime, the jet does not break into droplets and a continual flow of the dispersed phase in the continuous phase is achieved (from Nunes et al. 2010 [65]).

Droplet-based microfluidic techniques are widely used to fabricate alginate hydrogels, but many other cell or particle encapsulation techniques are based on droplet generation technology as well [55]. In these cases, the encapsulates are suspended in the aqueous dispersed phase, together with the hydrogel-forming materials like Matrigel or hyperbranched polyglycerol polyethylene glycol (hPG-PEG). Furthermore, the continuous or carrier phase, which needs to be immiscible or partially miscible with the aqueous dispersed phase, is often an oil [60]. Traditionally, hydrocarbon oils are used, such as mineral oil, but in many cell culturing applications, fluorinated oils are used because they are more soluble to gases such as oxygen and thus more biocompatible for cells. Often the oils are mixed with some type of surfactant, which reduces the surface tension between liquid-liquid interfaces and thus prevents the coalescence of droplets inside the microfluidic chip [60]. After the formation of the aqueous droplets inside the continuous phase, the gelation into hydrogel beads can be initiated either on-chip or after the droplets have been collected off-chip. In the case of alginate, an on-chip gelation technique could be the introduction of calcium ions after the formation of the droplets, whereas an off-chip technique would be collecting the droplets in a calcium bath. In the case of temperature-dependant agarose, the temperature can be precisely controlled inside the microfluidic chip using pre-heated liquids or heating elements. Finally, in

the case of photo-sensitive PEG polymers, including an optical window in the microfluidic chip and shining UV-light will induce PEG cross-linking. Each gelation technique has its own advantages and disadvantages, but due to relative ease of use, high control, low cost and ability to induce depletion interactions, alginate was chosen for this project.

1.4 PROJECT GOAL

The main goal of this thesis was to develop a new GV-based ultrasound contrast agent with improved echogenicity and longer circulation times compared to MBs and individual GVs. Specifically, the enhancement of nonlinear ultrasound contrast produced by these UCAs was of interest to promote their specific *in vivo* detection. To achieve this goal, a high-throughput microfluidic fabrication approach was explored. Aside from the reproducibility and a high droplet fabrication rate, microfluidics offer great control over the size and shape of the produced particles, as well as the number of encapsulated GVs in each particle. The final aim is to produce UCAs with diameters in the order of several microns, similar to that of conventionally used MBs, such that in the future they can become the go-to UCA for ultrasound applications such as fUS. Here, the aim was to encapsulate periodically aggregated GVs using a simple microfluidic device, and to investigate the acoustic properties of the fabricated particles.

In this work, GV aggregation was first studied in bulk through nonlinear ultrasound imaging of GVs, as well as with TEM imaging. Then, millimeter-sized mesoscale alginate beads containing GVs were fabricated and studied using ultrasound imaging. Finally, using a flow-focusing droplet-based microfluidic chip, microscale alginate beads containing GVs were fabricated. The fabricated beads were studied using phase contrast microscopy and ultrasound imaging.

2 MANUSCRIPT

The following pages contain the main body of this thesis, the manuscript, written in an article-style format.

Engineering of protein-based phononic crystals for contrast-enhanced ultrasound imaging

Juancito van Leeuwen[1,2], Dion Terwiel[1], Valeria Garbin[2], David Maresca[1]

1) Department of Imaging Physics, Delft University of Technology, The Netherlands

2) Department of Chemical Engineering, Delft University of Technology, The Netherlands

Abstract: Functional ultrasound imaging was recently introduced as a breakthrough hemodynamic imaging method capable of visualizing whole-brain neural activity with high spatiotemporal resolution. However, deep and transcranial monitoring of brain activity remains a challenge because of skull-induced attenuation of ultrasound waves. Clinically-approved microbubble (MB) contrast agents have been successfully used to raise hemodynamic contrast through the skull, but they add significant fluctuations to ultrasound signals and suffer from limited circulation times. A new class of genetically encoded acoustic contrast agents based on gas vesicle (GV) protein nanostructures have recently been shown to withstand higher acoustic pressures and provide smoother hemodynamic contrast than MBs. Despite these advantages, GVs are less echogenic than MBs, and are taken up by liver macrophages, which limits their circulation time. Here, we took the first step towards the development of an engineered GV-based ultrasound contrast agent with enhanced echogenicity and prolonged circulation time. We show that periodic aggregation of GVs using a depletant called alginate leads to a four-fold increase in nonlinear ultrasound contrast compared to unaggregated GVs. Moreover, we show that a high-throughput droplet-based microfluidic approach is capable of encapsulating GVs in 245 micron alginate hydrogel beads at a rate of 600 beads per second. Together, our results demonstrate a simple method to significantly enhance GV nonlinear contrast via periodic GV aggregation into protein-based phononic crystals, and pave the way for the high-throughput fabrication of biocompatible, GV-based ultrasound contrast agents using microfluidics.

Keywords: Gas vesicles, functional ultrasound imaging, droplet-based microfluidics, depletion interactions

I. Introduction

ULTRASOUND is one of the most widely used and versatile biomedical imaging modalities in clinical practice, which enables the assessment of organ anatomy and physiology with high spatial and temporal resolution [1]–[3]. Recently, functional ultrasound (fUS) imaging was introduced as a breakthrough imaging modality capable of mapping changes in local cerebral blood volume induced by neural activity [4]. Due to its portability, lower cost and spatiotemporal resolution an order of magnitude higher than functional MRI (fMRI), fUS has emerged as an attractive tool in neuroscience for visualizing whole-brain functional activity in various animal models and humans [5]–[11].

Transcranial fUS is limited in clinical applications due to aberrations caused by the skull, which render small blood flow variations indistinguishable from noise [12]. Therefore, most implementations currently rely on invasive surgical procedures involving craniotomies [4], thinned-skull preparations [13] or acoustically transparent windows [14].

The use of ultrasound contrast agents that enhance intravenous backscattering enables transcranial fUS without a skull preparation [13]. Clinically-approved lipid-shelled microbubbles (MBs) show high hemodynamic signal enhancement, but have the drawback of adding strong random fluctuations to signals which lowers the sensitivity of fUS imaging. These fluctuations likely arise from MB polydispersity, the lipid shell surface tension [15] and a variability in the acoustic response of MBs of a given size [16]. Moreover, MBs suffer from organ retention as well as gas escape and collapse upon ultrasound exposure, limiting their imaging time to several minutes [17].

A new class of hemodynamic ultrasound signal enhancers based on genetically encoded gas vesicles (GVs) has recently been introduced [18]. GVs are air-filled protein nanostructures with lengths in the order of 100–600 nm [19] and produce robust ultrasound contrast across medical ultrasound frequencies. Additionally, the biochemical composition and genetic encodability of GVs make it possible to engineer their mechanical, acoustical and physical properties, which allows for versatile and widely deployable contrast agents [20]–[22]. GVs can be engineered such that they exhibit nonlinear scattering behavior in response to acoustic pressures above their buckling threshold, enabling highly specific nonlinear imaging [23].

While providing smoother fUS signals and being able to withstand higher ultrasound pressures, GVs show lower ultrasound signal enhancement than MBs due to their nanoscale [24]. Furthermore, intravenously injected GVs are taken up by liver macrophages, which limits their circulation time in the blood stream to tens of minutes [25].

Here, we propose a novel ultrasound contrast agent consisting of periodically aggregated GVs encapsulated in microscale alginate beads. While GV aggregation has previously been shown to enhance ultrasound contrast [18], we hypothesize that ultrasound contrast can be maximized through periodic GV aggregation, analogous to phononic crystals [26]–[28]. Periodically assembled air-filled inclusions are capable of enhancing and suppressing acoustic waves at specific frequencies, through complex interactions involving multiple scattering reflections, nonlinear wave propagation and resonance [26], [27], [29]. Furthermore, alginate hydrogel encapsulation is conventionally used in biomedical and pharmaceutical industries to immobilize particles, improve their biocompatibility and prolong the circulation time of therapeutics in the blood stream [30]–[32].

The main goal of the work presented here is the exploration of an improved GV-based ultrasound contrast agent for fUS imaging. First, we investigated different GV aggregation strategies and their effect on the produced nonlinear acoustic

signal. Then, the effect of alginate encapsulation on GVs was studied in mesoscale beads. Finally, GVs were encapsulated in sub-millimeter-scale alginate beads using a flow-focusing microfluidic approach, capable of high-throughput, monodisperse droplet production. The fabricated alginate beads were studied acoustically via ultrasound imaging and optically using phase contrast microscopy.

II. Materials and Methods

Gas vesicle preparation

Wild-type GVs (WT GVs) were isolated and purified from *Anabaena flos-aqueae* cyanobacteria following a previously published protocol [33]. Nonlinear harmonic GVs (hGVs), GVs without the structural reinforcement protein GvpC on the outer surface, were prepared by adding a 6 M urea solution to WT GVs, followed by two rounds of centrifugally assisted purification. GV concentration was measured using optical density (OD) at 500 nm in a spectrophotometer (Ocean Insight, Orlando, FL, USA). For both WT and hGVs, OD = 1 is equal to 114 pM GV concentration in aqueous solution [33].

Gas vesicle aggregation

Periodic GV aggregation was achieved through depletion interactions. A depletion force is the effective attractive force that arises between impermeable particles when suspended in a solution of depletants, which are solutes that are preferentially excluded from the vicinity of the impermeable particles (Supplementary Figure S1a) [34]. The periodic stacking of cylindrical GVs eliminates the gaps between them, thereby creating more free space for depletants and maximizing translational entropy (Supplementary Figure S1b). The depletant used here was sodium alginate (M_w = 216.12 g mol^{-1}, Sigma-Aldrich, St. Louis, MO, USA), a biopolymer capable of forming biocompatible hydrogels through cross-linking when exposed to divalent cations such as Ca^{2+}. We expect GV (OD = 2) aggregation at alginate concentrations equal to and above 1.5 mg/ml, as GVs suspended in these solutions have an increased buoyancy likely related to aggregation (Supplementary Figure S2).

Nonperiodic GV aggregation was achieved by suspending GVs in a 100 mM solution of calcium chloride ($CaCl_2$, Sigma Aldrich, St. Louis, MO, USA) [34], or through GV biotinylation and subsequent addition of a 10,000 molar excess of streptavidin compared to GVs [18]. $CaCl_2$ and similar electrolytes induce GV aggregation by screening the net negative surface charge of GVs, allowing attractive Van der Waals interactions to form GV assemblies [34]. GV biotinylation was achieved using EZ-Link Sulfo-NHS-biotin (Thermofisher Scientific, Waltham, MA, USA) for four hours under gentle rotation, followed by two rounds of dialysis with HEPES buffer and two rounds of centrifugally assisted purification.

TEM

GV configurations were visualized via transmission electron microscopy (TEM) using a JEM-1400plus microscope (JEOL, Ltd., Tokyo, Japan) operating at 120 kV. Cu400 carbon support film TEM grids (Quantifoil Micro Tools GmbH, Großlöbichau, Germany) were first glow discharged using a GloQube glow discharge system (Quorum Technologies, Lewes, UK), rendering the grid surface hydrophilic. Then, 3.6 µl of GV solution (OD = 1) with HEPES buffer (control), 2 mg/ml alginate or 100 mM $CaCl_2$, or biotinylated GVs (OD = 1) with or without a 10.000 molar excess of streptavidin, was added to the TEM grid. After 1 minute, the solutions were removed through wicking with filter paper. In all but the case for alginate, a subsequent staining was performed by applying 3 µl of 2% uranyl acetate for 30 seconds to the grid. Alginate samples were not stained as the positive uranyl ions induce alginate gelation. All TEM grids were allowed to air-dry before imaging.

GV orientations in TEM images were quantified manually using the straight line selection tool of ImageJ (National Institutes of Health, Bethesda, MD) along the center line of each GV from cone tip to cone tip. The angles were normalized to 0° and subsequent polar histogram plots were made using MATLAB (The Mathworks, Inc., Natick, MA, USA).

Well phantom preparation

Ultrasound imaging phantoms were prepared by melting a 2% agarose (Thermofisher Scientific, Waltham, MA, USA) solution in buffer, which was poured into a DNA gel holder. A custom 3D-printed male mold was used to create cylindrical wells in the agarose of 5 mm in length, 2 mm in diameter and spaced 2 mm apart (Figure 1). GV samples were incubated at 45 °C for 1 minute after being mixed in a 1:1 ratio with 2% low melting temperature agarose (Thermofisher Scientific,

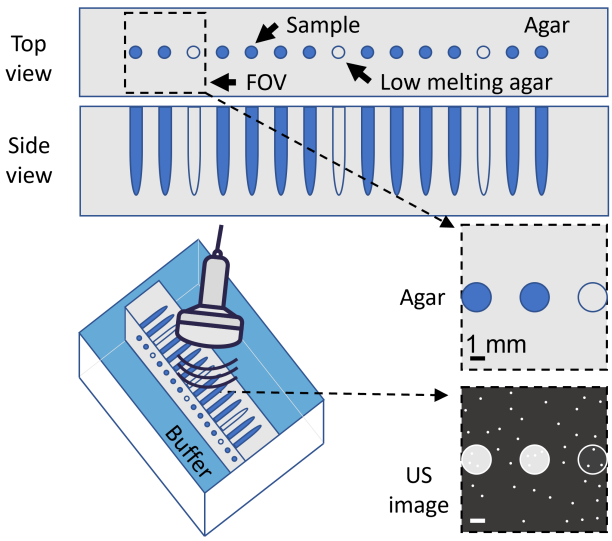

Fig. 1. **Phantom used for ultrasound characterization of GVs.** The wells are created by inserting a mold in liquid agarose, which is removed once the agarose has solidified. Wells can then be filled with either GV samples mixed with agarose (blue) or just agarose (gray), as displayed here, such that in every field-of-view (FOV) there is always at least 1 agarose well for background noise measurements. Once solidified, the phantom can then be imaged on its side to obtain ultrasound images of well cross sections.

Waltham, MA, USA) for a final GV concentration of OD = 2. Wells were then filled with 20 µl of GV sample or 1% low melting temperature agarose for background noise measurements, according to Figure 1.

Ultrasound imaging

Ultrasound imaging was performed using a Verasonics Vantage 256 channnel system with an L22-14V ultrasound probe (Verasonics Inc., Redmond, WA, USA). The probe is a linear array consisting of 128 elements with a 0.10 mm pitch, a 1.5 mm elevation aperture, an 8 mm elevation focus and a center frequency of 18.5 MHz (Vermon S.A., Tours, France). A custom imaging sequence was used, capable of both linear B-mode (brightness) ultrasound imaging and nonlinear cross-amplitude modulation (xAM) ultrasound imaging. In both cases, images were acquired with coherent compounding of 10.5, 16 and 21° angles. Raw RF data collected from 10 acquisitions per FOV was beamformed and summed offline. Circular background and GV sample regions of interest (ROI) with radii of 0.7 mm were manually selected at the middle of each well, at the same depth and taking care to avoid artifacts from the edges. Nonlinear ultrasound contrast-to-noise ratios (CNR) were quantified as the mean pixel intensity of the GV sample ROI divided by the mean pixel intensity of the background ROI. Conversion to decibels (dB) was calculated as $20*\log_{10}(\text{contrast})$, where log is the decimal logarithmic function. The dB values were subsequently visualized using box plots. For display, the background noise levels of the ultrasound images being compared were normalized, and the colormaps were set to range from 0 to 55 dB.

Microfluidic chip fabrication

The microfluidic chip that was used to fabricate GV-alginate beads consisted of two inlets, a flow-focusing double T junction and an outlet. The channel width at the inlets and outlet was 750 µm, while the width at the flow focusing junction was 125 µm (Supplementary Figure S3).

The master was fabricated by standard photolithography, as described before [35]. The PDMS-based microfluidic chips were made by pouring onto the master a layer of degassed PDMS precursor mixed in a 1:10 ratio with curing agent. The PDMS was allowed to cure at 70 °C for at least 3 hours before the PDMS with the chip pattern was lifted off the wafer. Meanwhile, glass slides were spin coated (90 seconds at 2000 rpm) with a 1:5 ratio mixture of PDMS and curing agent, and cured at 70 °C for 30 minutes. Bonding of the PDMS substrates to the PDMS-coated slides was achieved by fusing after plasma cleaning (Harrick Plasma Inc., Ithaca, NY, USA) and further curing overnight at 70 °C.

Alginate bead production and characterization

For the production of mesoscale beads, WT and hGVs (OD = 2), or HEPES buffer (control), were suspended in 1% alginate solution (∼10 mg/ml). The solutions were then gradually ejected from a syringe with a G23 needle into a bath of 0.5 M $CaCl_2$ at a height of 5 cm.

In the microfluidic approach, aqueous alginate and GV droplets were formed at the flow focusing orifice at the center of the microfluidic device, where an interface was created between two immiscible fluids: a dispersed and continuous phase. The dispersed phase consisted of a 1% sodium alginate solution mixed with either WT or hGVs (OD = 2), or buffer. The continuous phase consisted of Novec 7500 Engineered Fluid (3M, Saint Paul, MN, USA) with 0.1% Picosurf surfactant (Sphere Fluidics, Ltd., Cambridge, UK). The solutions were supplied to their respective inlets by means of syringes attached to programmable syringe pumps (Harvard Apparatus, Holliston, MA, USA) (Supplementary Figure S3). The continuous phase was supplied to the outer inlet at a flowrate of Q_c = 1800 µl h^{-1}, while the dispersed phase was supplied to the inner inlet at a flowrate of Q_d = 50 µl h^{-1}. These flowrates allowed for reliable fabrication of droplets. Lower flowrates and Q_c:Q_d flowrate ratios led to larger droplets, while higher flowrates caused overpressures inside the chip. The syringes were connected to polytetrafluoroethylen (PTFE) tubes (0.8 mm ID x 1.6 mm OD) with syringe tube connectors.

The process of droplet formation was observed and recorded using a DFK 33UX273 camera (The Imaging Source, Bremen, Germany) attached to an inverted optical microscope (Euromex Microscopen B.V., Arnhem, The Netherlands). Droplet fabrication rate was estimated manually based on the movies acquired with the camera. Once formed, the droplets flowed through the channel towards the outlet, and were collected in a beaker with 0.5 M $CaCl_2$ via PTFE tubes. The calcium bath allowed for quick gelation of the alginate into hydrogel beads. After 1 hour of fabrication, the beads were strained and washed with $CaCl_2$ three times using Fisherbrand cell strainers (Thermofisher Scientific, Waltham, MA, USA) with 100 µm pore size, and stored at 4 °C.

The mesoscale beads were observed acoustically with linear B-mode and nonlinear xAM ultrasound imaging after trapping them in a 2% agarose phantom. The microscale beads were observed both acoustically, via the well phantom approach described before, using linear B-mode and nonlinear xAM ultrasound imaging, and optically, using an IX71 inverted light microscope (Olympus Corp., Tokyo, Japan) with a 20x phase contrast objective and DCC1645C digital camera (Thorlabs Inc., Newton, NJ, USA). Phase contrast microscopy was chosen since GVs have been shown to produce positive phase contrast [36], [37]. This was confirmed by comparing OD = 2 WT GVs pre- and post collapse (Supplementary Figure S4). Average bead diameters for droplet-shaped meso- and microscale beads were estimated by considering only the spherical part of each bead.

III. Results

GV aggregation characterization

GVs were aggregated using three methods: fusion proteins (biotin + streptavidin), ionic screening ($CaCl_2$), and depletion interaction (alginate).

TEM images of hGVs in 2 mg/ml of alginate showed that alginate induces periodic GV aggregation, while biotinylated hGVs with a 10.000 molar excess of streptavidin and hGVs in

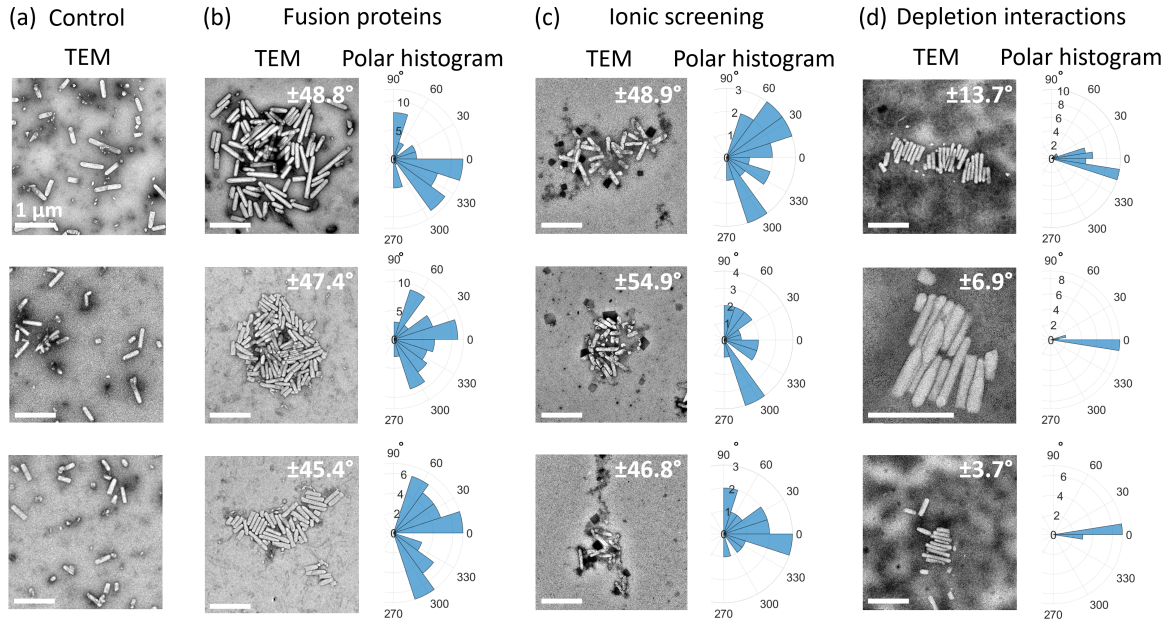

Fig. 2. **Engineered aggregation of purified GVs.** (a) hGVs in HEPES buffer (control) show no aggregation when observed with TEM. (b) Biotinylated hGVs with a 10.000 molar excess of streptavidin and (c) hGVs in 100 mM $CaCl_2$ are aggregated in random configurations, demonstrated by the wide distribution of GV angles in the polar histograms. (d) hGVs in 2 mg/ml alginate are aggregated periodically, which is confirmed by the narrow distribution of angles centered around 0° in the polar histogram. Values at the top right of each TEM image indicate the standard deviation of angles in each assembly. Scale bars represent 1 µm. The middle $CaCl_2$ TEM image (c) as well as all control (a) and biotin + streptavidin (b) images were digital zooms from the original images.

100 mM $CaCl_2$ aggregate in seemingly random configurations (Figure 2). We have quantified the periodicity of the aggregates using normalized angular distributions in polar histograms. The standard deviation of the angles of GVs in alginate in each assembly (±13.7°, ±6.9° and ±3.7°) are roughly six times lower than the standard deviations for biotin + streptavidin (±48.8°, ±47.4° and ±45.4°) and for $CaCl_2$ (±48.9°, ±54.9° and ±46.8°). Periodic aggregation was also observed for WT GVs suspended in alginate (Figure S5).

Aggregation-induced nonlinear contrast enhancement

Aggregated hGVs were loaded into agarose phantoms and imaged using xAM ultrasound imaging (Figure 3). Randomly aggregated GVs ($CaCl_2$ and biotin + streptavidin) show an increase in contrast of approximately 6 dB over the control. For periodically aggregated GVs, a nonlinear ultrasound contrast enhancement of 12 dB over the control was observed (8.0 dB to 20.1 dB), indicating that periodicity of aggregation has a substantial effect on hGV aggregate nonlinear contrast. We confirmed that the contrast enhancement observed for biotinylated GVs mixed with streptavidin is due to aggregation in a control experiment where we omitted streptavidin (Supplementary Figure S6).

We have previously observed that the buoyancy of GVs is enhanced at alginate concentrations at or above 1.5 mg/ml (Supplementary Figure S2). We hypothesise that the increased buoyancy is a consequence of GV aggregation and an alginate concentration of 1.5 mg/ml is therefore the minimal aggregation inducing concentration. To confirm these observations

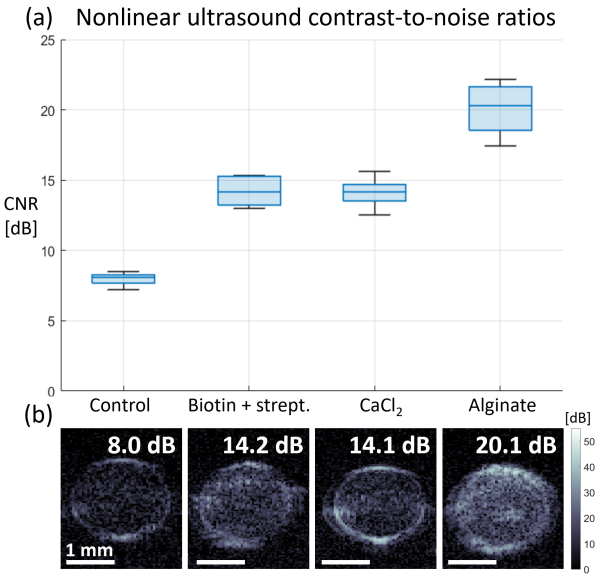

Fig. 3. **Nonlinear ultrasound contrast enhancement through hGV aggregation.** (a) Box plots showing the CNRs for hGVs (OD = 2) in buffer (control), biotinylated hGVs with 10.000 molar excess of streptavidin, hGVs in 100 mM $CaCl_2$ and hGVs in 2 mg/ml alginate. Lower and upper box boundaries represent the 25th and 75th percentiles, while the middle line represents the median. Lower and upper error lines represent the 10th and 90th percentiles. (b) Representative xAM ultrasound images of the samples from (a). Values at the top right of each ultrasound image indicate the average CNR per sample. Periodically aggregated GVs in alginate show a larger increase in CNR over the control than the biotinylated GVs in streptavidin and GVs in $CaCl_2$. Scale bars represent 1 mm. In all cases, N = 8.

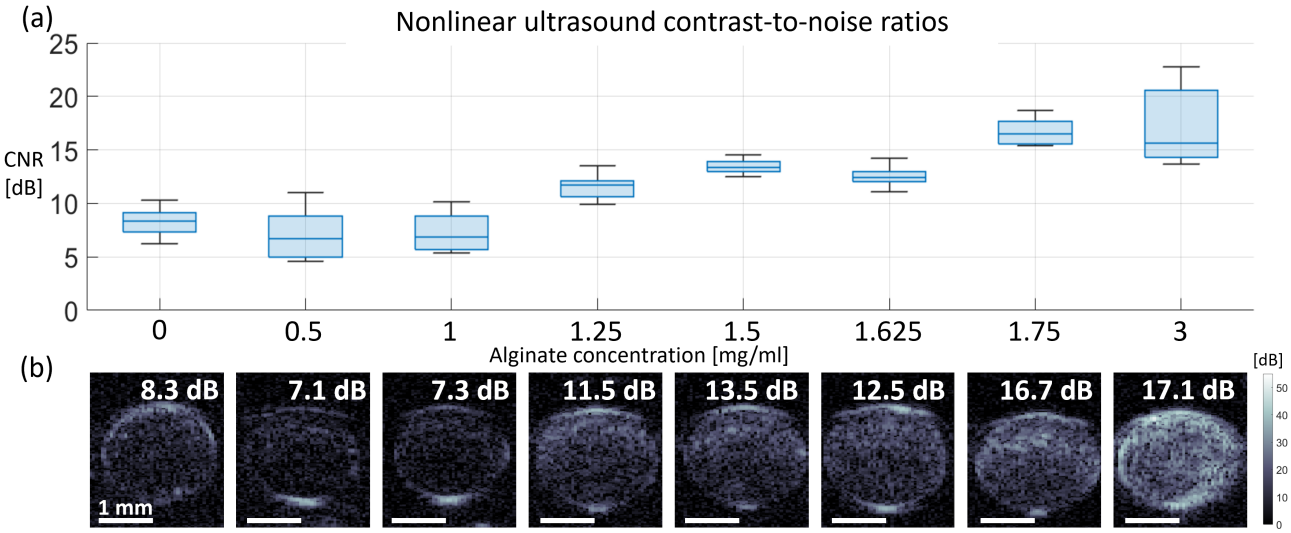

Fig. 4. **Influence of alginate concentration on nonlinear contrast enhancement.** (a) Box plots showing the CNRs for hGVs (OD = 2) in concentrations of alginate varying from 0 to 3 mg/ml. Lower and upper box boundaries represent the 25th and 75th percentiles, while the middle line represents the median. Lower and upper error lines represent the 10th and 90th percentiles. (b) Representative xAM ultrasound images of each sample from (a). Values at the top right of each ultrasound image indicate the average CNR per sample. An increase in CNR of 3 dBs over the control is seen starting at 1.25 mg/ml alginate. Scale bars represent 1 mm. In all cases, N = 8, except for 3 mg/ml (N = 6).

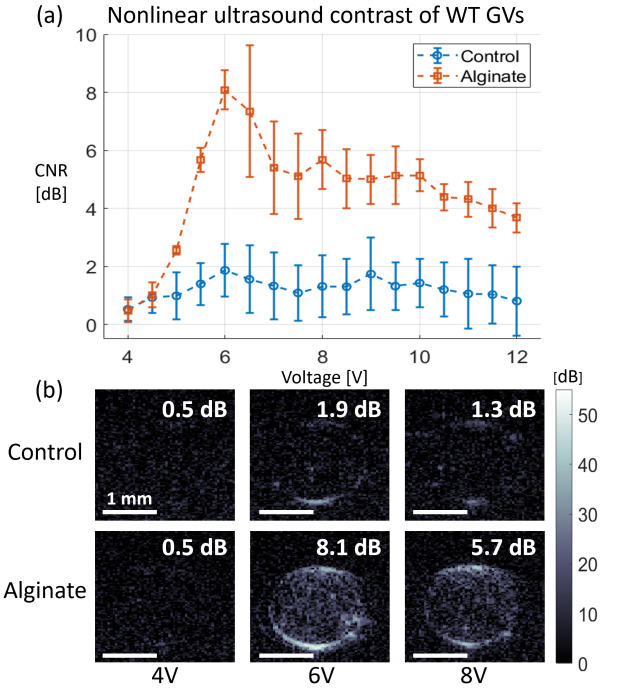

Fig. 5. **Nonlinear response of periodically aggregated wild-type GVs.** (a) Average CNRs for WT GVs (OD = 2) in buffer (control) and 2 mg/ml alginate as a function of transducer transmit voltage. Errorbars indicate standard deviations. (b) Representative xAM ultrasound images of wells filled with WT GVs in buffer (control, top row) or 2 mg/ml alginate (bottom row), at 4, 6 and 8V. Values at the top of each ultrasound image indicate the average CNR of that sample at that particular voltage. At 6 V, a maximum CNR of 8 dB is reached for periodically aggregated (Figure S5) WT GVs, while the maximum CNR for the control is 2 dB at 6.5 V. Scale bars represent 1 mm. N = 3 for the control and N = 4 for WT GVs in alginate.

we imaged hGVs (OD = 2) in varying concentrations of alginate (Figure 4). It can be observed that the threshold alginate concentration for OD = 2 GV depletion interactions is roughly 1.25 mg/ml, as the contrast increase is 3 dBs compared to lower concentrations and the control. At 1.75 mg/ml of alginate, a plateau in contrast enhancement is reached.

WT GVs typically do not show nonlinear contrast, as their increased stiffness prevents significant buckling beneath the collapse pressure threshold. However, we observed that when suspended in 2 mg/ml of alginate, periodically aggregated WT GVs display a clear increase in nonlinear contrast over the control (Figure 5). This increase is observed between transducer transmit voltages of 5 V - 12 V, with a maximum contrast difference of ∼6 dB at 6 V. After 6 V, a decrease in CNR is observed, which for WT GVs in alginate plateaus at 5 dB.

Together, these results demonstrate that alginate-induced periodic GV aggregation remarkably enhances the nonlinear ultrasound contrast produced by hGVs. Nonlinear ultrasound contrast enhancement was also observed for periodically aggregated WT GVs in alginate.

GV encapsulation in alginate beads

The next step, once periodic GV aggregation was achieved and nonlinear ultrasound contrast enhancement was observed, was to encapsulate periodically aggregated GVs. Encapsulation was performed at two scales: initially, mesoscale beads were made using a syringe and a calcium bath, followed by microscale beads made using a microfluidic chip.

Ultrasound imaging showed that the mesoscale beads were teardrop-shaped and roughly 2 mm in diameter for each sample (Figure 6). The beads containing hGVs appeared in both linear B-mode and nonlinear xAM imaging modes, whereas

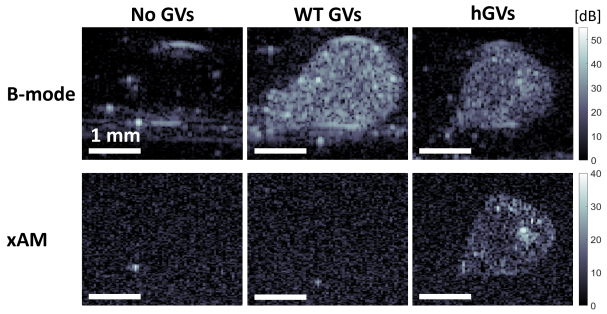

Fig. 6. **Ultrasound imaging of mesoscale alginate beads.** Top row: linear B-mode ultrasound images of an empty bead and beads containing WT and hGVs, respectively. Bottom row: nonlinear xAM ultrasound images of the same three beads. WT GVs in alginate beads only appear in linear B-mode images, while hGVs appear in both linear B-mode and nonlinear xAM images. The interface of the bead without GVs faintly appears in linear B-mode images and does not appear in nonlinear xAM images. Scale bars represent 1 mm.

the beads containing WT GVs only appeared in the linear imaging mode. Empty alginate beads were not visible in the nonlinear imaging mode, while only the interface appeared in the linear imaging mode.

In the microfluidic approach, spherical, monodisperse droplets in the order of 125 µm were observed inside the microfluidic chip through an inverted optical microscope. The droplets were generated at a rate of 600 beads per second (Figure 7a). Once gelated, the microscale beads had various different shapes, as observed with phase contrast microscopy (Figure 7b and Supplementary Figure S7). The average final bead size was 241 µm for beads without GVs, 248 µm for the beads containing WT GVs and 245 µm for the beads containing hGVs. Phase contrast microscope images show the presence of GVs inside the beads, since GVs are capable of producing positive phase contrast and appear white in a transparent background. Conversely, the beads without GVs did not show any white contrast. Moreover, when using a higher concentration of GVs, the final beads appeared more crowded and were larger in size (Supplementary Figure S8). Using linear B-mode ultrasound imaging, both beads containing WT or hGVs and the empty beads were observed in the longitudinal section of agarose well phantoms as bright point-source scatterers, while the well without beads appeared empty (Figure 7c). All three beads were faintly visible in nonlinear xAM imaging at a transducer transmit voltage of 15 V, compared to the well without beads. Futhermore, the bright scattering was observed before and after exposure to high GV-collapse-inducing pressures (Supplementary Figure S9).

In summary, the ultrasound images of the mesoscale beads show the successful encapsulation of WT and hGVs, while phase contrast microscopy images confirm the encapsulation of WT and hGVs in microscale alginate beads. However, ultrasound imaging of the microscale alginate beads could not verify this as the control empty beads were also observed and ultrasound signal from GV-containing beads persisted after GV-collapse-inducing pressures.

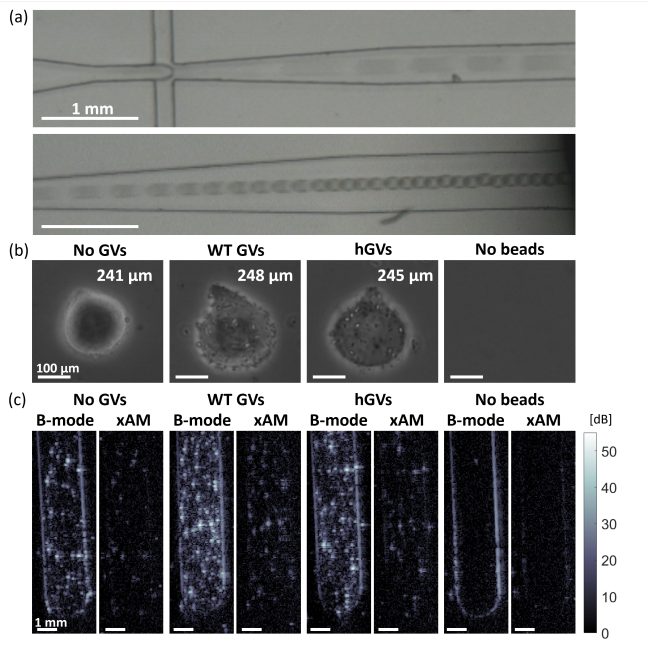

Fig. 7. **Microfluidic fabrication of microscale alginate beads.** (a) Two single frame snapshots through an inverted light microscope showing droplet generation and flow at the flow focusing orifice (top) and the end of the microfluidic chip (bottom). (b) Phase contrast microscopy images of a bead without GVs, beads containing hGVs and WT GVs, respectively, and the empty background. WT and hGVs appear white in phase contrast microscopy, while the empty beads show no white contrast. Values at the top represent average bead size (N = 10), considering only the spherical part of teardrop-shaped beads. (c) Linear B-mode and nonlinear xAM ultrasound images taken along the long side of wells containing the three different beads from (c) and a well containing only agarose. All three beads appear in linear B-mode images as bright point-source scatterers, while a well filled with agarose is empty. All beads appeared in nonlinear xAM images when transmitting at 15 V. Scale bars in panel (a) and (c) represent 1 mm, and scale bars in panel (b) represent 100 µm.

IV. Discussion

Our results establish a platform for the fabrication of novel GV-based ultrasound contrast agents with enhanced echogenicity and potentially prolonged circulation time in the blood stream.

In vitro experiments confirmed our hypothesis that GVs aggregate into periodic assemblies when suspended in a solution of alginate above a threshold concentration, likely due to depletion interactions [34]. Moreover, we show that periodically aggregated hGVs produce notably higher nonlinear ultrasound contrast enhancement than hGVs aggregated in random configurations (20 dB versus 14 dB). This is equal to a four-fold increase in linear scale units compared the control. We hypothesize that this stark contrast enhancement arises from multiple scattering of the ultrasound wave in these periodic air-filled assemblies analogous to phononic crystals [26], [27]. As these interactions significantly increase the mean free path of the ultrasound wave in the periodic GV medium, ultrasound waves of a high enough pressure may build up higher harmonics over time due to nonlinear wave propagation [38].

We show that nonlinear contrast enhancement starts at an alginate concentration of 1.25 mg/ml for GVs at OD = 2

(equal to 224 pM GV concentration [33]). Therefore, this is roughly the alginate concentration threshold at which depletion interactions start to occur among GVs at this OD. Higher concentrations of alginate showed an increase in CNR, until a plateau was reached at 1.75 mg/ml. Yao et al. [34] have shown using dynamic light scattering (DLS) that GV assembly size is directly related to depletant concentration. Therefore, the increase in contrast and subsequent plateau we observe is possibly due to an increase in GV assembly size, until a maximum size is reached. In the future, this will need to be confirmed by supporting TEM images and DLS measurements.

Furthermore, our results show that periodically aggregated WT GVs in alginate show a large increase in nonlinear ultrasound contrast compared to the control at higher transmit voltages (+6 dB at 6 V). The increase in contrast is likely due to the same increased number of multiple scattering events as in the case of hGVs. Ultrasound nonlinearity scales with the pressure of the transmitted wave, which is proportional to the transducer transmit voltage. Therefore, the ultrasound nonlinearity only becomes observable once the transducer voltage is high enough. The observed nonlinear contrast even persisted at higher voltages, at which WT GVs usually collapse. A reason for this could be the presence of smaller, more resilient bicones in the solution.

Following the *in vitro* GV experiments, we showed two techniques for isolating and immobilizing GV aggregates in alginate hydrogel beads. First, WT and hGVs were encapsulated in mesoscale alginate beads and were characterized with ultrasound imaging. The empty alginate beads did not appear in either imaging mode, while both types of GV-containing beads appeared in linear ultrasound imaging and only the hGVs appeared in xAM ultrasound imaging. These results confirm that the GVs were encapsulated and did not collapse during alginate cross-linking. However, these results do not directly indicate that the GVs inside the alginate beads are still aggregated periodically. This needs to be confirmed in the future, through high resolution optical imaging techniques such as fluorescent microscopy of labeled GVs or scanning electron microscopy of sectioned beads.

Finally, microscale beads were fabricated using a high-throughput droplet-based microfluidic technique. Through phase contrast microscopy, a clear distinction was seen between the beads containing either the WT or hGVs, which showed white contrast, compared to the empty alginate beads. The microscale alginate beads had various different shapes, with an average final size in the order of 245 µm. The size and shape seen after gelation is contrary to the 125 µm spherical droplets inside the microfluidic chip. This is likely due to the gelation strategy, since the off-chip gelation of alginate droplets in divalent ion baths creates polydisperse beads with variable shapes, depending on many parameters [39].

The ultrasound images of these beads were inconsistent with our mesoscale findings, as both the GV-containing and the empty beads showed similar echogenecities. A similar result was obtained in the nonlinear imaging mode at a relatively high transmit voltage of 15 V. WT and hGVs typically collapse at 6 and 4.5 V respectively, so the bright reflections in the images likely do not originate from GVs. A possible explanation for all three beads to appear as bright point-source scatterers in ultrasound images is that microscopic air-filled cavities could form inside the alginate beads during gelation at the surface of the calcium bath [40]. Furthermore, the relatively low density of bright pixels in the wells filled with beads compared to homogenously bright GV-filled wells of previous experiments is likely due to the low concentration of alginate beads in the final solution after filtering.

In future work, other microfluidic chip designs and alginate gelation strategies should be explored to overcome the aforementioned issues. On-chip alginate gelation strategies have been shown to produce beads with little variability in size and shape [41], and will likely prevent the formation of air-filled cavities in the alginate beads upon gelation. Without the need for a divalent ion bath, the collected solution will have a higher concentration of alginate beads. Furthermore, smaller microfluidic chip dimensions and techniques that utilize solvent extraction have been shown to create alginate beads of several microns, similar to that of conventionally used MB contrast agents [42].

V. Conclusion

To conclude, our results demonstrate the remarkable increase in nonlinear contrast produced by GVs when aggregated periodically. Moreover, using a high-throughput microfluidic approach, we fabricated sub-millimeter-scale GV-containing alginate beads at a fast rate. Further engineering of the microfluidic encapsulation strategy could shrink the size of these novel ultrasound contrast agents to the same size as conventional MBs, and prevent unwanted air-filled cavities.

Once the size of the alginate beads has been reduced to the order of several microns, and *in vitro* ultrasound experiments have confirmed their enhanced echogenicity, *in vivo* studies should be performed to confirm the prolonged circulation time of these alginate beads in the blood stream.

In the future, these novel, GV-based ultrasound contrast agents with enhanced echogenicity, reduced random signal fluctuations and prolonged circulation times can become the go-to hemodynamic enhancers for non-invasive transcranial fUS imaging as well as other contrast-enhanced ultrasound imaging applications. For example, genetic and biochemical engineering of GV acoustic and targeting properties could allow for highly specific molecular imaging of enzyme activity and sensing changes in pH caused by inflammation.

Acknowledgments

We thank Stefan Huber and Arjen Jakobi for helpful discussions and access to the TEM. We would also like to thank Pouyan Boukany, Kristen David, Zaid Rahman and Margherita Tavasso for access to and their help in the microfluidics lab. Moreover, we thank Olivia Weidlich, Rick Waasdorp and Baptiste Heiles for creating and improving the wide-FOV xAM imaging script. Finally, we would like to thank Tarannum Ara for preparing and isolating all GV solutions. We acknowledge support from the Dutch Research Council (NWO.STU019.021 to DM) and the Delft Bioengineering Institute (to VG and DM).

REFERENCES

[1] H. D. Liang, J. Alison Noble, and P. N. Wells, "Recent advances in biomedical ultrasonic imaging techniques," *Interface Focus*, vol. 1, no. 4, pp. 475–476, 2011.

[2] M. Tanter and M. Fink, "Ultrafast imaging in biomedical ultrasound," *IEEE Transactions on Ultrasonics, Ferroelectrics, and Frequency Control*, vol. 61, no. 1, pp. 102–119, 2014.

[3] B. Heiles, D. Terwiel, and D. Maresca, "The Advent of Biomolecular Ultrasound Imaging," *Neuroscience*, pp. 1–12, 2021.

[4] E. Mace, G. Montaldo, I. Cohen, M. Baulac, M. Fink, and M. Tanter, "Functional ultrasound imaging of the brain," *Nature Methods*, vol. 8, no. 8, pp. 662–664, 2011.

[5] É. Mace, G. Montaldo, S. Trenholm, C. Cowan, A. Brignall, A. Urban, and B. Roska, "Whole-Brain Functional Ultrasound Imaging Reveals Brain Modules for Visuomotor Integration," pp. 1241–1251.e7, 2018.

[6] A. Urban, E. Mace, C. Brunner, M. Heidmann, J. Rossier, and G. Montaldo, "Chronic assessment of cerebral hemodynamics during rat forepaw electrical stimulation using functional ultrasound imaging," *NeuroImage*, vol. 101, pp. 138–149, 2014.

[7] E. Tiran, J. Ferrier, T. Deffieux, J. L. Gennisson, S. Pezet, Z. Lenkei, and M. Tanter, "Transcranial Functional Ultrasound Imaging in Freely Moving Awake Mice and Anesthetized Young Rats without Contrast Agent," *Ultrasound in Medicine and Biology*, vol. 43, no. 8, pp. 1679–1689, 2017.

[8] R. Rau, P. Kruizinga, F. Mastik, M. Belau, N. de Jong, J. G. Bosch, W. Scheffer, and G. Maret, "3D functional ultrasound imaging of pigeons," *NeuroImage*, vol. 183, no. July, pp. 469–477, 2018.

[9] C. Bimbard, C. Demene, C. Girard, S. Radtke-Schuller, S. Shamma, M. Tanter, and Y. Boubenec, "Multi-scale mapping along the auditory hierarchy using high-resolution functional ultrasound in the awake ferret," *eLife*, vol. 7, pp. 1–14, 2018.

[10] K. Blaize, F. Arcizet, M. Gesnik, H. Ahnine, U. Ferrari, T. Deffieux, P. Pouget, F. Chavane, M. Fink, J. A. Sahel, J. A. Sahel, J. A. Sahel, M. Tanter, and S. Picaud, "Functional ultrasound imaging of deep visual cortex in awake nonhuman primates," *Proceedings of the National Academy of Sciences of the United States of America*, vol. 117, no. 25, pp. 14 453–14 463, 2020.

[11] S. Soloukey, A. J. Vincent, D. D. Satoer, F. Mastik, M. Smits, C. M. Dirven, C. Strydis, J. G. Bosch, A. F. van der Steen, C. I. De Zeeuw, S. K. Koekkoek, and P. Kruizinga, "Functional Ultrasound (fUS) During Awake Brain Surgery: The Clinical Potential of Intra-Operative Functional and Vascular Brain Mapping," *Frontiers in Neuroscience*, vol. 13, no. January, pp. 1–14, 2020.

[12] G. Pinton, J. F. Aubry, E. Bossy, M. Muller, M. Pernot, and M. Tanter, "Attenuation, scattering, and absorption of ultrasound in the skull bone," *Medical Physics*, vol. 39, no. 1, pp. 299–307, 2012.

[13] C. Errico, B. F. Osmanski, S. Pezet, O. Couture, Z. Lenkei, and M. Tanter, "Transcranial functional ultrasound imaging of the brain using microbubble-enhanced ultrasensitive Doppler," *NeuroImage*, vol. 124, pp. 752–761, 2016.

[14] T. Deffieux, C. Demene, M. Pernot, and M. Tanter, "Functional ultrasound neuroimaging: a review of the preclinical and clinical state of the art," *Current Opinion in Neurobiology*, vol. 50, pp. 128–135, 2018.

[15] B. Helfield, "A Review of Phospholipid Encapsulated Ultrasound Contrast Agent Microbubble Physics," *Ultrasound in Medicine and Biology*, vol. 45, no. 2, pp. 282–300, 2019.

[16] M. Emmer, H. J. Vos, M. Versluis, and N. D. Jong, "Radial modulation of single microbubbles," *IEEE Transactions on Ultrasonics, Ferroelectrics, and Frequency Control*, vol. 56, no. 11, pp. 2370–2379, 2009.

[17] J. E. Chômas, P. Dayton, J. Alien, K. Morgan, and K. W. Ferrara, "Mechanisms of contrast agent destruction," *IEEE Transactions on Ultrasonics, Ferroelectrics, and Frequency Control*, vol. 48, no. 1, pp. 232–248, 2001.

[18] M. G. Shapiro, P. W. Goodwill, A. Neogy, M. Yin, F. S. Foster, D. V. Schaffer, and S. M. Conolly, "Biogenic gas nanostructures as ultrasonic molecular reporters," *Nature Nanotechnology*, vol. 9, no. 4, pp. 311–316, 2014.

[19] A. E. Walsby, "Gas vesicles," *Microbiological Reviews*, vol. 58, no. 1, pp. 94–144, 1994.

[20] A. Lakshmanan, A. Farhadi, S. P. Nety, A. Lee-Gosselin, R. W. Bourdeau, D. Maresca, and M. G. Shapiro, "Molecular Engineering of Acoustic Protein Nanostructures," *ACS Nano*, vol. 10, no. 8, pp. 7314–7322, 2016.

[21] A. Farhadi, G. H. Ho, D. P. Sawyer, R. W. Bourdeau, and M. G. Shapiro, "Ultrasound imaging of gene expression in mammalian cells," *Science*, vol. 365, no. 6460, pp. 1469–1475, 2019.

[22] A. Lakshmanan, Z. Jin, S. P. Nety, D. P. Sawyer, A. Lee-Gosselin, D. Malounda, M. B. Swift, D. Maresca, and M. G. Shapiro, "Acoustic biosensors for ultrasound imaging of enzyme activity," *Nature Chemical Biology*, vol. 16, no. 9, pp. 988–996, 2020.

[23] D. Maresca, A. Lakshmanan, A. Lee-Gosselin, J. M. Melis, Y. L. Ni, R. W. Bourdeau, D. M. Kochmann, and M. G. Shapiro, "Nonlinear ultrasound imaging of nanoscale acoustic biomolecules," *Applied Physics Letters*, vol. 110, no. 7, pp. 1–5, 2017.

[24] D. Maresca, T. Payen, A. Lee-Gosselin, B. Ling, D. Malounda, C. Demené, M. Tanter, and M. G. Shapiro, "Acoustic biomolecules enhance hemodynamic functional ultrasound imaging of neural activity," *NeuroImage*, vol. 209, no. November 2019, pp. 0–7, 2020.

[25] B. Ling, J. Lee, D. Maresca, A. Lee-Gosselin, D. Malounda, M. B. Swift, and M. G. Shapiro, "Biomolecular Ultrasound Imaging of Phagolysosomal Function," *ACS Nano*, vol. 14, no. 9, pp. 12 210–12 221, 2020.

[26] V. Leroy, A. Bretagne, M. Fink, H. Willaime, P. Tabeling, and A. Tourin, "Design and characterization of bubble phononic crystals," *Applied Physics Letters*, vol. 95, no. 17, pp. 1–4, 2009.

[27] P. A. Deymier, *Acoustic metamaterials and phononic crystals*. Springer Heidelberg, 2013.

[28] L. Chinchilla, C. Armstrong, R. Mehri, A. S. Savoia, M. Fenech, and E. Franceschini, "Numerical investigations of anisotropic structures of red blood cell aggregates on ultrasonic backscattering," *The Journal of the Acoustical Society of America*, vol. 149, no. 4, pp. 2415–2425, 2021.

[29] A. Bretagne, A. Tourin, and V. Leroy, "Enhanced and reduced transmission of acoustic waves with bubble meta-screens," *Applied Physics Letters*, vol. 99, no. 22, pp. 5–7, 2011.

[30] K. Y. Lee and D. J. Mooney, "Alginate: Properties and biomedical applications," *Progress in Polymer Science (Oxford)*, vol. 37, no. 1, pp. 106–126, 2012.

[31] D. Dhamecha, R. Movsas, U. Sano, and J. U. Menon, "Applications of alginate microspheres in therapeutics delivery and cell culture: Past, present and future," *International Journal of Pharmaceutics*, vol. 569, no. May, p. 118627, 2019.

[32] T. Hu and A. C. Lo, "Collagen–alginate composite hydrogel: Application in tissue engineering and biomedical sciences," *Polymers*, vol. 13, no. 11, 2021.

[33] A. Lakshmanan, G. J. Lu, A. Farhadi, S. P. Nety, M. Kunth, A. Lee-Gosselin, D. Maresca, R. W. Bourdeau, M. Yin, J. Yan, C. Witte, D. Malounda, F. S. Foster, L. Schröder, and M. G. Shapiro, "Preparation of biogenic gas vesicle nanostructures for use as contrast agents for ultrasound and MRI," *Nature Protocols*, vol. 12, no. 10, pp. 2050–2080, 2017.

[34] Y. Yao, Z. Jin, B. Ling, D. Malounda, and M. G. Shapiro, "Self-assembly of protein superstructures by physical interactions under cytoplasm-like conditions," *Biophysical Journal*, vol. 120, no. 13, pp. 2701–2709, 2021.

[35] R. Seemann, M. Brinkmann, T. Pfohl, and S. Herminghaus, "Droplet based microfluidics," *Reports on Progress in Physics*, vol. 75, no. 1, 2012.

[36] A. Farhadi, M. Bedrossian, J. Lee, G. H. Ho, M. G. Shapiro, and J. L. Nadeau, "Genetically Encoded Phase Contrast Agents for Digital Holographic Microscopy," *Nano Letters*, 2020.

[37] A. Bar-Zion, A. Nourmahnad, D. R. Mittelstein, S. Shivaei, S. Yoo, M. T. Buss, R. C. Hurt, D. Malounda, M. H. Abedi, A. Lee-Gosselin *et al.*, "Acoustically triggered mechanotherapy using genetically encoded gas vesicles," *Nature Nanotechnology*, vol. 16, no. 12, pp. 1403–1412, 2021.

[38] T. L. Szabo, *Diagnostic Ultrasound Imaging: Inside out*, 2nd ed. Elsevier Academic Press, 2014.

[39] Y. Hu, Q. Wang, J. Wang, J. Zhu, H. Wang, and Y. Yang, "Shape controllable microgel particles prepared by microfluidic combining external ionic crosslinking," *Biomicrofluidics*, vol. 6, no. 2, pp. 1–9, 2012.

[40] F. Stops, J. T. Fell, J. H. Collett, and L. G. Martini, "Floating dosage forms to prolong gastro-retention—the characterisation of calcium alginate beads," *International journal of pharmaceutics*, vol. 350, no. 1-2, pp. 301–311, 2008.

[41] A. Moreira, J. Carneiro, J. B. Campos, and J. M. Miranda, "Production of hydrogel microparticles in microfluidic devices: a review," *Microfluidics and Nanofluidics*, vol. 25, no. 2, pp. 1–24, 2021.

[42] A. Pittermannová, Z. Ruberová, A. Zadražil, N. Bremond, J. Bibette, and F. Štěpánek, "Microfluidic fabrication of composite hydrogel microparticles in the size range of blood cells," *RSC Advances*, vol. 6, no. 105, pp. 103 532–103 540, 2016.

APPENDIX

Supplementary figures

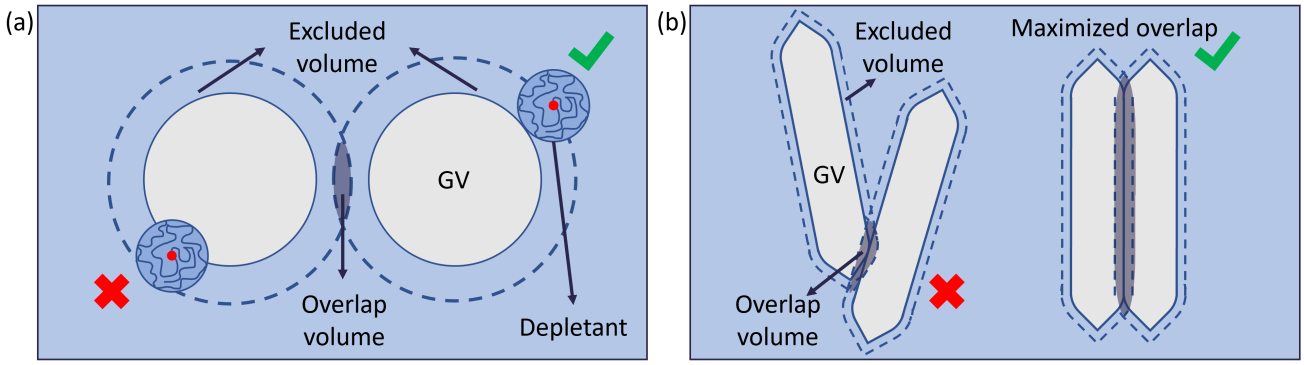

Fig. S1. **Schematic representation of depletion interactions on GVs.** (a) Depletants such as alginate are preferentially excluded from the vicinity (i.e. the excluded volume) of impermeable GVs. (b) To minimize the gap between GVs and thus maximize the free space for depletants, maximal overlap of the excluded volume is achieved through periodic, side-by-side stacking.

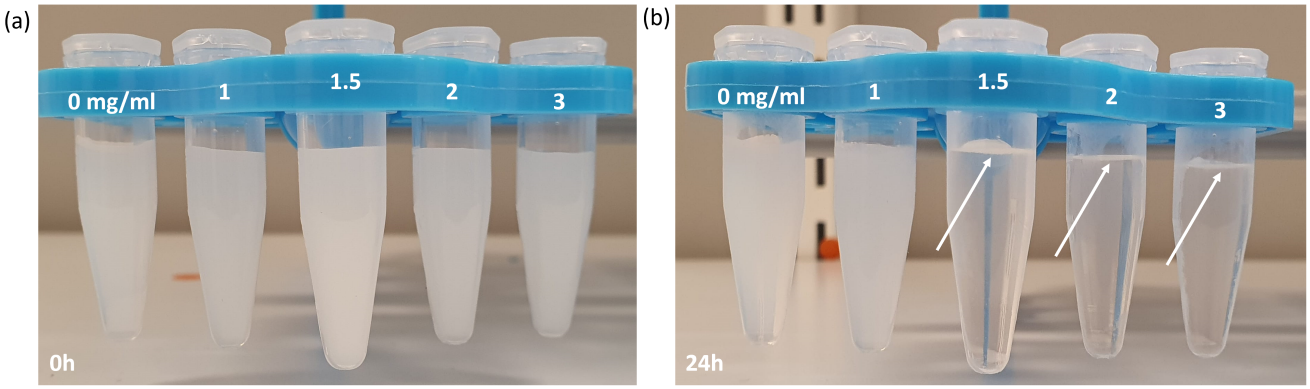

Fig. S2. **GVs suspended in different concentrations of alginate at 0h and 24h after suspension.** (a) hGVs (OD = 2) in HEPES buffer, and 1, 1.5, 2 and 3 mg/ml alginate at 0h and (b) after 24h. GVs have an enhanced buoyancy when suspended in alginate solutions at and above 1.5 mg/ml, which is likely related to aggregation. White arrows highlight the floating layer of GVs.

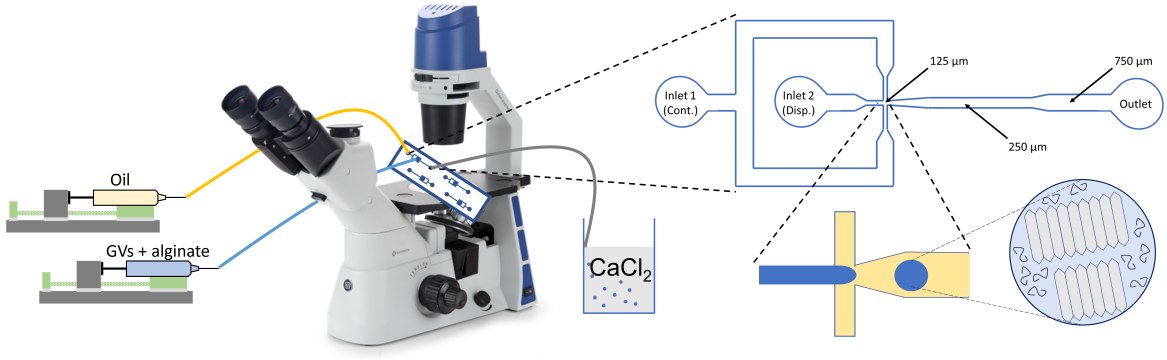

Fig. S3. **Sketch of the microfluidic bead fabrication setup and the flow focusing chip design used for droplet generation.** The continuous phase (oil and surfactant) is supplied to inlet 1 and the dispersed phase (alginate with or without WT or hGVs) is supplied to inlet 2. The flowrates are controlled using syringe pumps. Droplets are collected from the outlet in a calcium bath.

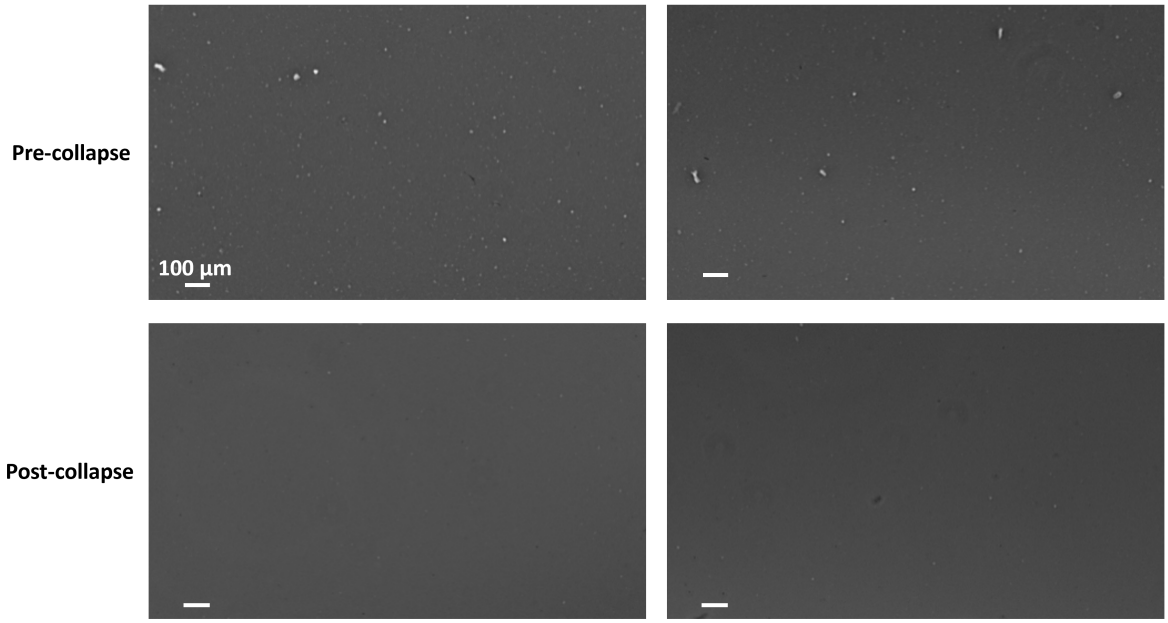

Fig. S4. **Phase contrast microscopy images of WT GVs pre- and post collapse.** Using phase contrast microscopy, OD = 2 WT GVs were compared before and after collapse. GV collapse was induced by applying 10 bar hydrostatic pressure to the solution. Pre-collapse, white contrast is observed in the phase contrast microscopy images, whereas the white contrast is absent in the post-collapse images.

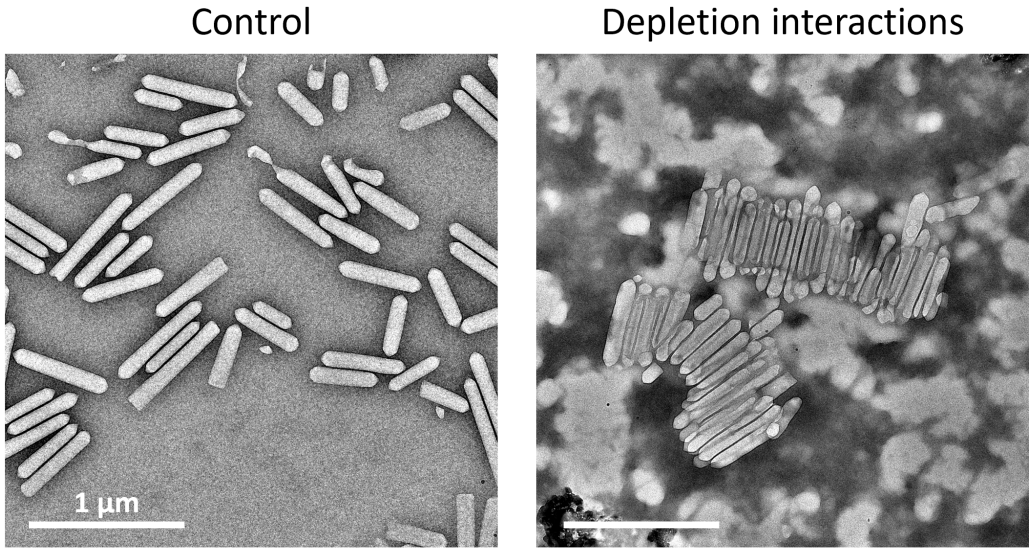

Fig. S5. **Alginate-induced periodic WT GV aggregation.** TEM images of WT GVs (OD = 1) suspended in 1 mg/ml alginate show periodic GV aggregation when compared to the control, similar to hGVs (Figure 2). Scale bars represent 1 µm.

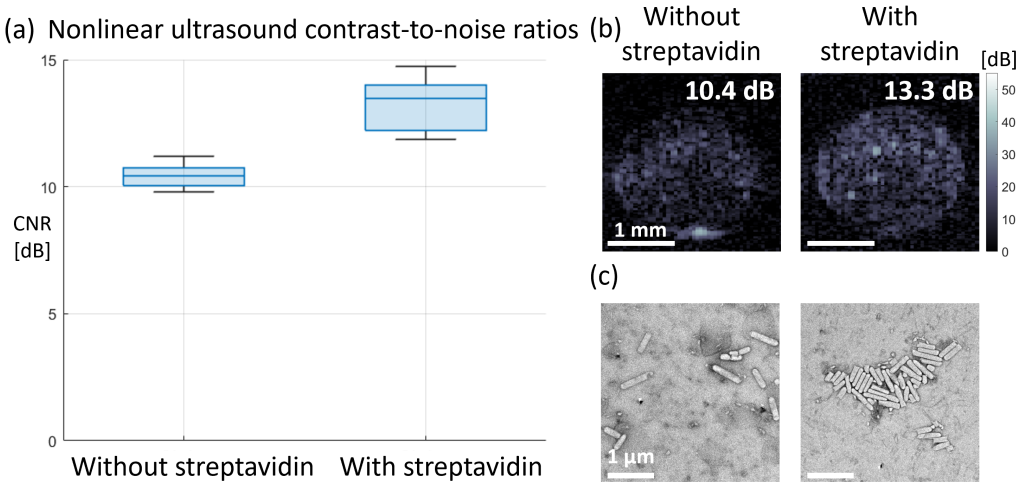

Fig. S6. **Nonlinear ultrasound contrast for biotinylated GVs with and without streptavidin.** (a) Box plots of the CNR values for biotinylated hGVs (OD = 2) with and without a 10.000 molar excess of streptavidin. Lower and upper box boundaries represent the 25th and 75th percentiles, while the middle line represents the median. Lower and upper error lines represent the 10th and 90th percentiles. (b) Representative xAM ultrasound images and (c) TEM images of the samples described above. Streptavidin induces aggregation of biotinylated GVs, which enhances nonlinear ultrasound contrast by 3 dB compared to unaggregated biotinylated hGVs. Values in the top right corner of each ultrasound image indicate the average contrast per sample. Scale bars in ultrasound images represent 1 mm, while in TEM images they represent 1 µm. In all cases, N = 8.

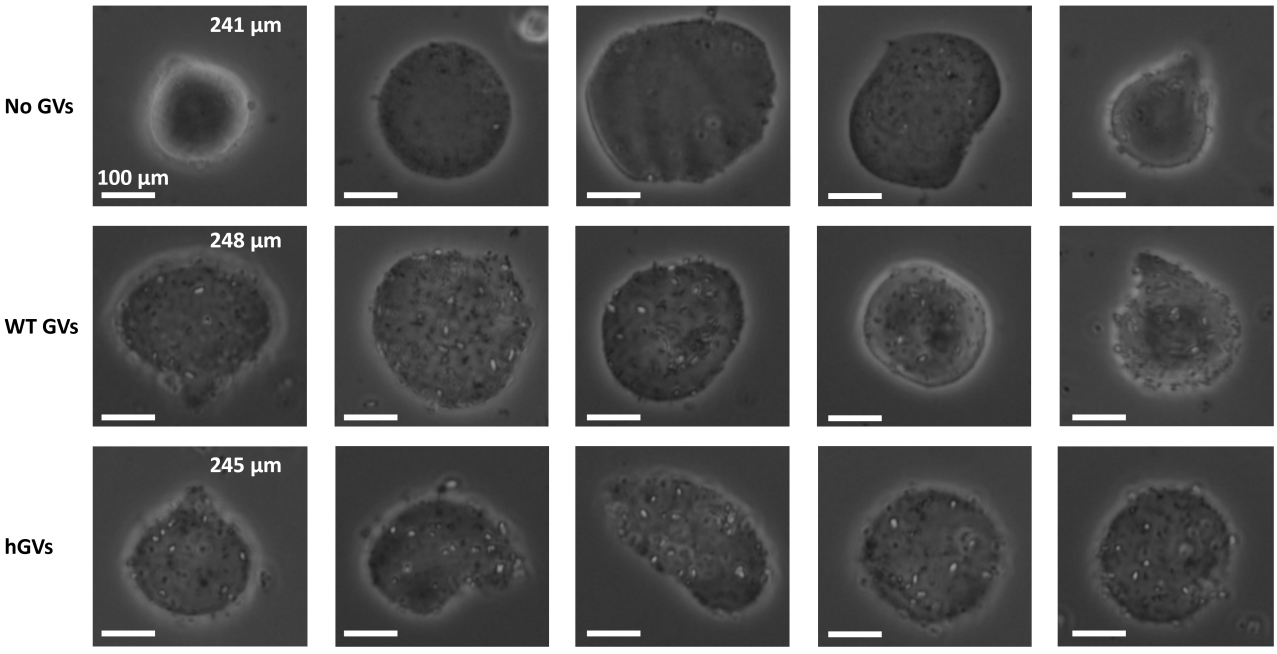

Fig. S7. **Phase contrast microscopy images of microscopic beads.** Top row: beads without GVs. Middle row: beads with WT GVs (OD = 2). Bottom row: beads with hGVs (OD = 2). Beads containing GVs showed the presence of GVs as white contrast, whereas the beads without GVs appeared empty. The beads had various shapes and sizes. Values in the top right of the first column indicate the average size of N = 10 beads. Scale bars represent 100 µm.

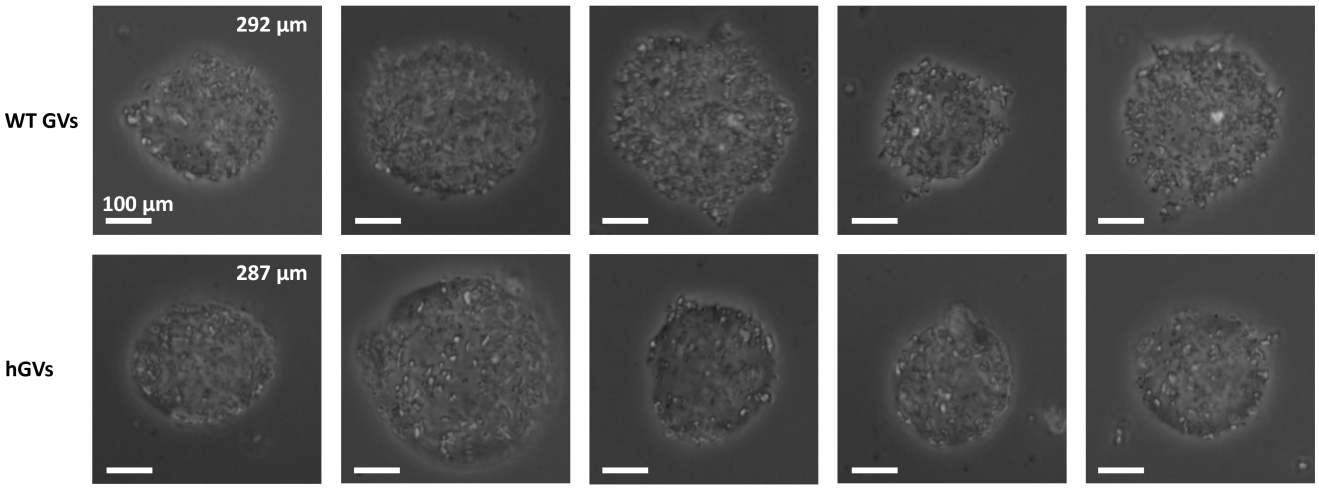

Fig. S8. **Phase contrast microscopy images of microscopic beads containing OD 8 WT and hGVs.** Top row: beads with WT GVs. Bottom row: beads with hGVs. Beads containing a higher OD GVs appear more crowded, but were also larger than beads with OD = 2 GVs. Values in the top right of the first column indicate the average size of N = 10 beads. Scale bars represent 100 µm.

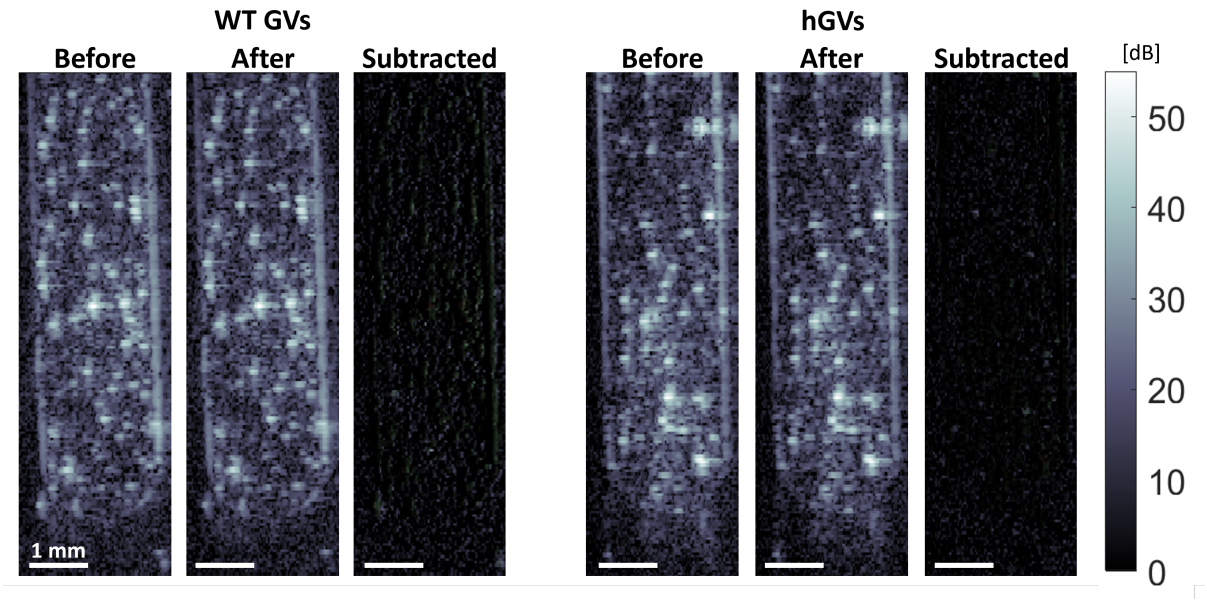

Fig. S9. **Linear B-mode ultrasound images of GV-containing beads.** Cross sections along the long edge of a well containing beads with encapsulated WT GVs (left) and hGVs (right) before and after exposure to high pressure waves, and the subtraction of the two images. Since the before and after images appear identical and GVs typically collapse at the high pressure waves corresponding to a 15 V transducer voltage, the bright point-source scattering observed in the ultrasound images likely does not originate from GVs. Scale bars represent 1 mm.

3 DISCUSSION AND OUTLOOK

The main aim of this project was the development of a new GV-based ultrasound contrast agent with improved properties compared to individual GVs and MBs. Specifically, novel UCAs were desired with improved echogenicity and prolonged circulation times in the blood stream. To achieve this goal, a high-throughput microfluidic fabrication approach was implemented for greater control over particle size and shape, reproducibility and high production rate. The aim was to fabricate alginate beads containing encapsulated GVs and to characterize their acoustic properties.

3.1 GV AGGREGATION EXPERIMENTS

First, to enhance GV echogenicity, multiple GV aggregation strategies were studied as well as their effect on ultrasound contrast enhancement. The results from chapter 2 show that alginate-induced periodic GV aggregation, which likely arises from depletion interactions, maximizes the available nonlinear ultrasound contrast-to-noise ratio (CNR), compared to random GV aggregation by biotinylation or $CaCl_2$. The effect of dextran and NaCl on GV aggregation were also studied as alternative depletant and electrolyte (section A.1). However, alginate showed a higher reproducibility than dextran and has the advantage of hydrogel formation.

The physical mechanisms explaining the remarkable nonlinear ultrasound contrast enhancement from periodically aggregated GVs that has been observed experimentally will need to be investigated in a follow-up study. A possible explanation is that the mean free path of an ultrasound wave propagating in a periodic GV assembly is greatly enhanced due to multiple reflections compared to the mean free path of a wave in an unordered GV assembly, leading to the build up of higher harmonic frequencies during wave propagation at high amplitude. While it has been shown that GVs derived from other microbes than *Anabaena flos-aquae*, such as *Serratia sp. 39006* GVs, produce an enhanced nonlinear ultrasound contrast [37], no strategies to date have been reported that enhance GV nonlinear scattering as much as shown here. In future work, it would be interesting to see if the periodic aggregation of *Serratia* GVs would also lead to enhanced nonlinear ultrasound contrast, and how that would compare to Ana hGVs.

The alginate concentration of 1.25 mg/ml at which nonlinear ultrasound CNR increase was observed for hGVs at OD = 2 is estimated to be the threshold concentration at which depletion interactions between GVs start to occur. It has been shown that the free energy of a pair of GVs becomes more negative at higher depletant concentrations, which induces stable GV assembly. In this thesis, a higher increase in nonlinear ultrasound CNR for GVs at higher concentrations of alginate was observed. Judging by the increase in assembly size seen at a higher depletant concentration in Yao et al. [49], the increase in nonlinear ultrasound CNR presented here is likely due to an increased GV assembly size or an increased number of GV assemblies. The similarity in CNR between 1.75 and 3 mg/ml alginate appears as a plateau, suggesting that a maximum assembly size or number of assemblies has been reached.

However, ultrasound contrast is an indirect measure of GV aggregation, and using a more direct measure such as assembly size through TEM or dynamic light scattering (DLS) could prove to be more accurate. Unfortunately, several attempts at both were unsuccessful (section A.2), mainly due to the viscosity of alginate. Highly

viscous alginate solutions proved difficult to remove from TEM grids by wicking. Moreover, solution viscosity plays an important role in DLS measurements, but little is known in the literature about the viscosity of alginate at such low concentrations (below 5 mg/ml). In the future, supporting evidence of GV assembly size for nonlinear ultrasound contrast enhancement should be acquired for more reliable conjectures. Lower OD GVs and thus lower alginate concentrations could, for example, be explored to reduce viscosity-related issues.

The results from Yao et al. [49] show that the trends of assembly growth with depletant concentration were highly similar for both WT and hGVs, which suggests that the depletion interactions are independent of the presence of GvpC protein on the outer shell. This was confirmed with TEM images of periodically aggregated WT GVs in alginate. The large increase in nonlinear CNR observed of WT GVs in alginate at 6 V is likely caused by the same phenomenon as observed in hGVs; a prolonged travel path inside the GV assemblies leads to a build-up of ultrasound wave nonlinearity.

3.2 GV ENCAPSULATION IN ALGINATE BEADS

After the characterization of nonlinear ultrasound contrast enhancement by periodic aggregation of GVs, GVs were immobilized in alginate hydrogel beads of two different scales. It was a priori unknown whether encapsulation and cross-linking of alginate would have an influence on GV stability. Ultrasound images of mesoscale encapsulated beads seem to indicate no significant loss of signal and, consequently, no loss of stability of the GVs during encapsulation.

Subsequently, a simple high-throughput droplet-based microfluidic technique was used to fabricate microscopic alginate beads. Observation of droplet formation in the microfluidic device proved challenging as the fast combined flowrate of 1850 µl h^{-1} meant that the camera (300 fps) was not able to film highly resolved individual droplets inside of the microfluidic channel. Near the end of the microfluidic chip, the droplets were less smeared and tracking of individual droplets was easier, allowing for the estimation of the droplet fabrication rate.

Once collected at the outlet, the droplets were gelated off-chip in a calcium bath. However, the relatively large volume of the calcium solution led to a low concentration of beads. In the current setup, to increase the alginate bead concentration as well as to separate them from the oil phase, the collected beads were filtered using strainers. While this led to slightly higher alginate bead concentrations, not all beads could successfully be removed from the strainers and this method added significant variation in the final bead concentration of each sample. Alternative solid/liquid separation methods might be more efficient, such as centrifugal separation. Methods that cause overpressures should be avoided to prevent GV collapse, so low accelerations should be used in the case of centrifugal separation. Alternatively, an on-chip gelation strategy would remove the need for a calcium bath and therefore increase the concentration of collected beads in the final solution.

Ultrasound images of the microscopic alginate beads were taken along the long edge of the wells rather than through the cross-section, since this allowed for a larger view of the considerably low density of scatterers inside each well. No CNRs were calculated for two reasons. First, valid CNRs require noise and signal region-of-interest (ROI) to be at the same depth due to depth-dependent ultrasound signal attenuation. This was not possible since there was little space beside the well in this field-of-view for a noise ROI. Second, calculating CNRs typically requires a homogeneous distribution of bright pixels, which was not the case for the low concentration of beads. In the future, when higher concentrations of alginate beads are acquired, imaging should be performed along the cross-section of the agarose well phantoms, such that reliable background noise estimates can be measured and multiple slices along each well can be imaged.

Unfortunately, the ultrasound images of the microscopic beads were inconclusive concerning GV stability post-encapsulation. Bright point-source scatterers can be observed in the ultrasound images of all three beads, even after high GV-collapse-inducing pressures. The observed ultrasound signal therefore likely does not originate from GVs. One possible explanation for the high echogenicity of the alginate beads is the presence of air-filled cavities inside the beads [66]. These might have arisen during alginate gelation at the surface of the calcium bath, since there is no air present inside the microfluidic chip. A solution to this problem would be to use an on-chip alginate gelation strategy such that the alginate beads are not exposed to air pre-gelation. As an alternative ultrasound imaging strategy for the agarose well phantom, imaging of the beads in a flow phantom was explored to avoid agarose-alginate bead interfaces. Here, the alginate beads were imaged after injection into a 1 cm well filled with buffer inside of an agarose slab (section A.3). However, all three types of beads appeared in both linear B-mode and nonlinear xAM ultrasound imaging, similar to the well phantom approach. The observed reflections seen in the well phantom approach are therefore unlikely to arise from the agarose-alginate bead interface.

Phase contrast microscopy [67] offered a better look at the fabricated beads, both quantitatively for the bead size, as well as qualitatively for the bead shape and presence of GVs. The fabricated microscale beads appeared slightly larger than inside the microfluidic chip, likely by aggregation of the aqueous droplets inside of the microfluidic tubing and the expansion of the droplets once released into the calcium bath. Moreover, the beads often appeared droplet-shaped, which is also a direct cause of the release from the tubing into the calcium bath. Both the change in size and shape compared to pre-gelation can thus be attributed to the gelation strategy. When using an ion bath, the final shape and size can vary largely and depend on many factors, including the ion concentration and viscosity of the calcium bath [68]. Therefore, an alternative on-chip gelation strategy should be investigated to ensure reliable and reproducible alginate bead size and shape.

The difference in bead size of the GV-containing beads compared to the empty bead is related to the addition of GVs to the alginate solution, since all other experimental conditions were the same. The added GVs likely increased the density or apparent viscosity of the dispersed phase, which led to larger droplets in the microfluidic chip. Similarly, the white contrast only seen in the phase contrast microscopy images of both the GV-containing beads can likely be attributed to the presence of the GVs, as demonstrated in earlier studies [69, 70]. These results therefore suggest the successful encapsulation of GVs in the chip. In the future, evidence still needs to be found to prove that the GVs are periodically aggregated inside of the alginate beads, as the GV orientation could possibly have changed during alginate gelation. One possible way to do this is through single-molecule localization microscopy techniques after fluorescent labeling of the encapsulated GVs.

3.3 FINAL RECOMMENDATIONS AND OUTLOOK

The solutions of microscale alginate beads fabricated in this thesis exhibited variable and relatively low bead concentrations, featured beads that likely contained air-filled cavities, and that had relatively large sizes and variable shapes. As explained above, all of these issues can be addressed by use of an on-chip alginate gelation strategy. The introduction of calcium ions to the continuous phase downstream of the flow-focusing junction, for example, induces alginate cross-linking inside of the microfluidic chip. This creates spherical, monodisperse alginate beads inside the chip and removes the need for a calcium bath, thereby leading to a higher alginate bead concentration as well as preventing air-filled cavities. However, the main drawback of on-chip gelation strategies is the possibility of channel clogging,

so great care must be taken in tuning the final flow rates and solution concentrations.

To reach the final size goal of several microns, smaller channel dimensions could be investigated, as well as continuous phase injection angles below 90°. Solvent extraction techniques have also been shown to significantly reduce the size of alginate beads [71–73]. Using a continuous phase with non-negligible water solubility, water from the aqueous dispersed phase droplets can be extracted and dissolved into the continuous phase, thereby reducing the overall droplet volume. This has the direct effect of increasing the alginate concentration inside the droplet. Typically, a 1 mg/ml alginate solution is required for effective gelation. Therefore, a lower alginate concentration at the start of droplet generation could be used to reach this final alginate concentration after droplet shrinkage. A lower alginate concentration would mean a lower dispersed phase viscosity, which in turn leads to smaller droplets being fabricated at the flow-focusing junction. Another consequence of lower alginate concentrations in the dispersed phase is that a concentration below the depletion interaction threshold for GVs can be used. Unaggregated GVs in the dispersed phase offers more reliable control over the concentration of GVs inside the droplets upon formation, as the GVs are homogeneously mixed in the solution rather than in aggregated assemblies. By tuning the retention time of the alginate droplets inside of the continuous phase, the user has more control over the final bead size. With longer channels, for example, the droplets will have a longer retention time in the chip, leading to more water being extracted and thus smaller droplets. The microfluidic alginate encapsulation strategy proposed by Pittermanova et al. [73] uses 1-undecanol as the continuous phase, in which the solubility of water is roughly 2.7% v/v at room temperature, while the solubility of 1-undecanol in water is negligble. Downstream of droplet formation, calcium ions are introduced to the continuous phase to initiate alginate cross-linking, but the concentration of alginate at this point is too low for sufficient gelation. The retention time of droplets in 1-undecanol is prolonged using a serpentine structure to ensure droplet shrinkage and complete alginate gelation. Using an initial alginate concentration of 0.1 mg/ml, they managed to fabricate alginate beads in the order of 5 µm, with encapsulated liposomes and magnetic nanoparticles. Several attempts were made at recreating these results with encapsulated GV beads in the order of 5 µm. Unfortunately, these initial attempts were unsuccessful due to channel blockages (section A.4), but follow-up experiments or alternative solvent extraction techniques are recommended in the future to reach the final goal size of several microns.

Once monodisperse, spherical, GV-containing alginate beads of several microns in size have successfully been fabricated using an on-chip gelation microfluidic chip, the next step would be to characterize their acoustic properties. The high nonlinear ultrasound contrast observed in chapter 2 applied to GVs in bulk, and has not yet been studied for GVs in alginate beads. Therefore, the fabricated beads should be investigated with ultrasound imaging and could be compared to alginate beads containing randomly aggregated biotinylated GVs in streptavidin and clinically-available MBs. Specifically, the linear and nonlinear ultrasound contrast should be investigated at different ultrasound frequencies. A flow phantom similar to Maresca et al. [8] could also be used to characterize the flow detection limit of ultrasound imaging enhanced with the fabricated GV-based UCAs.

So far, an improved biocompatibility and prolonged circulation times in the blood stream provided by the alginate hydrogel have only been assumed and still need to be investigated. Therefore, once their acoustic properties have been characterized, *in vivo* experiments should be performed on animal models. The duration of ultrasound contrast could be compared between the fabricated alginate beads, unencapsulated GVs and MBs, making sure that the total gas fraction in each of these cases is the same for comparison. Simultaneously, the relative ultrasound contrast should be compared as well as the sensitivity of transcranial fUS measurements.

If *in vitro* and *in vivo* studies successfully prove the enhanced echogenicity and prolonged circulation time of these novel GV-based UCAs, they can become the go-to UCAs for CEUS and specifically fUS. Finally, through biochemical and genetic engineering of the GVs before encapsulation, these UCAs can be used for various other applications such as the detection of enzyme activity or inflammation-induced pH changes. These GV-based UCAs have the potential to become the most robust and versatile UCAs used in biomedical imaging.

A INSIGHTS GAINED FROM ADDITIONAL EXPERIMENTS AND ALTERNATIVE METHODS

The results shown in chapter 2 form the basis of a novel GV-based UCA with enhanced echogenicity and prolonged circulation time in the blood stream. What follows in this chapter are additional experiments that were performed and results that do not directly contribute to the results of the thesis but have produced interesting considerations to keep in mind for future work. First, the use of dextran and NaCl to aggregate GVs will be explained. Then, several performed DLS measurements and TEM images of GV assemblies will be discussed. Next, an alternative strategy for the imaging of microscopic alginate beads will be shown. Finally, attempts at fabricating microscopic alginate beads using a more complex microfluidic chip will be discussed.

A.1 DEXTRAN AND NACL-INDUCED GV AGGREGATION

Yao et al. [49] showed that dextran induces periodic GV aggregation, likely through depletion interactions. Therefore, GVs suspended in 550 kDa dextran (Sigma-Aldrich, St. Louis, MO, USA) were also imaged with xAM ultrasound imaging (Figure A.1a). In the resulting images, a pronounced, bright ring was observed at the edge of the wells, which was not the case for GVs in alginate. This is likely due to the relatively lower viscosity of dextran compared to alginate. A 1% solution of alginate (equal to roughly 10 mg/ml) has an average viscosity of 22.5 cP. However, a significantly higher concentration of 10% 500 kDa dextran has a viscosity of 30 cP [74]. Even though a lower concentration is required to aggregate GVs using alginate (1.25 mg/ml at OD = 2 compared to 50 mg/ml dextran at OD = 1, according to Yao et al. [49]), the alginate solution was notably more viscous. This higher viscosity likely limits GV mobility in the well before the agarose has completely set. With lower viscosities, it is possible for GVs to migrate to the edges of the wells due to the diffusion of water from the aqueous agarose solution inside the well to the dehydrating bulk of the agarose phantom. While GVs in alginate are likely also to migrate due to this effect, the migration occurs much slower than the gelating rate of the agarose because of the high viscosity of alginate. Regardless, after these observations, a solution was adopted and the agarose well phantom filling procedure was changed. Rather than filling the wells of the phantom on the bench top, the phantom was placed in a small layer of buffer, such that the agarose could stay moisturized and not absorb excess liquid from inside the wells. Immediately after the wells have been filled and also during ultrasound imaging, the phantoms were kept in a buffer solution. While this solution prevented the formation of bright rings at the edges of the wells containing GVs in dextran, subsequent depletion interaction experiments were carried out using only alginate due to its ability to form hydrogels.

As an alternative for $CaCl_2$, the electrolyte NaCl was also used to aggregate GVs in random configurations. However, the monovalence of sodium led to the need for a higher concentration of NaCl to achieve the same effect as divalent calcium ions in $CaCl_2$ [49]. The disadvantage of using concentrated solutions of salt (above 0.5 M NaCl) is the formation of salt-based artefacts during TEM imaging (Figure A.1b).

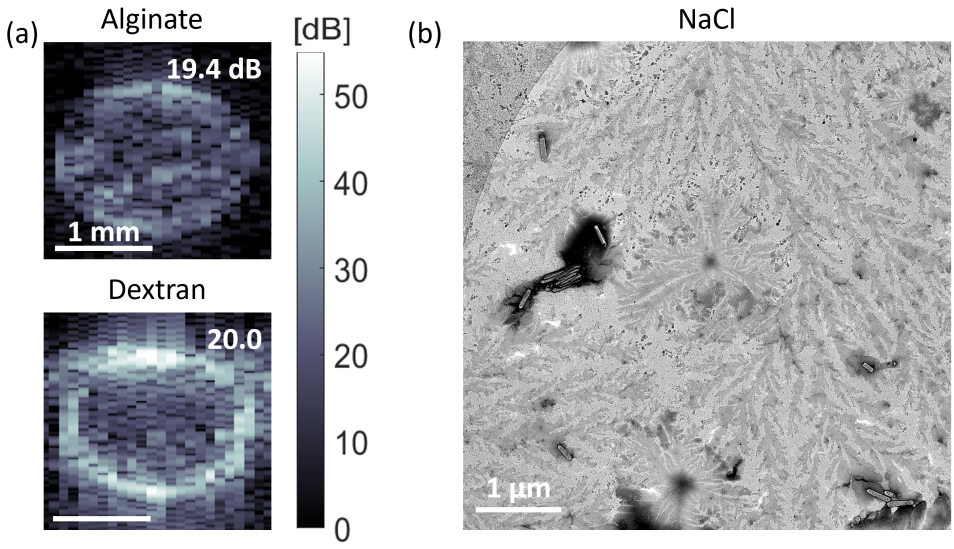

Figure A.1: GV aggregation with alginate, dextran and NaCl. (a) In nonlinear xAM ultrasound images, a bright ring appears surrounding wells filled with GVs in dextran, which does not appear in the case of GVs in alginate. Values at the top right of each ultrasound image indicate the average CNR per sample (N = 5). (b) High concentrations of NaCl led to salt-based artefacts in TEM images. Scale bars represent 1 mm in ultrasound images and 1 µm in the TEM image.

A.2 AGGREGATION CHARACTERIZATION USING DLS AND TEM

In chapter 2, ultrasound imaging imaging was used as an indirect measure to characterize GV aggregation at various alginate concentrations. A clear increase in nonlinear contrast can be seen with increasing alginate concentrations, which is similar to the DLS results of Yao et al. [49], relating the hydrodynamic radii of GV assemblies to the concentrations of various salts and dextran. Therefore, the nonlinear ultrasound CNR increase is likely related to the GV assembly size.

Several attempts were made at a direct measure of GV assembly size as a function of alginate concentration, using both DLS and TEM. DLS is a well-established technique for determining the size distribution of small nanoscale particles in suspension, by measuring the temporal fluctuations in the light scattered by the sample. Light scattered off small particles, which can undergo fast diffusion through a medium, will have much larger fluctuations than slower diffusing large particles [75]. Sample viscosity plays a large role in this, since it can influence the particle diffusion rate. A higher viscosity slows down particle diffusion, and therefore, small particles will appear larger if this is not taken into account. Unfortunately, no information is available in the literature on the viscosity of alginate at concentrations between 0.5 and 3 mg/ml, making it difficult to accurately measure the hydrodynamic radii of individual GVs or GV assemblies in alginate. Even so, an attempt was made at measuring particle size by reducing the GV concentration such that the difference in viscosity between the different alginate concentrations was likely negligible. Assuming that the depletion interaction threshold concentration scales linearly with OD, the tested alginate concentrations at OD = 0.25 were 0, 0.125, 0.15625, 0.1875, 0.21875, 0.25 and 0.375 mg/ml, and an extreme case of 5 mg/ml at which a viscosity of 5 cP was estimated. Each sample was loaded into disposable cuvettes, which were placed in a Malvern Zetasizer Nano ZS (Malvern Panalytical Ltd., Malvern, UK). For each concentration, 2 samples were measured 3 times (N = 6), each measurement lasting 60 seconds. For the 5 mg/ml alginate sample, a

background viscosity of 5 cP was chosen, while for all other mentions the viscosity of water was chosen (0.89 cP). The results show no increase in particle size at and above 0.15625 mg/ml, which corresponds to 1.25 mg/ml for OD = 2 GVs (Figure A.2a). This is likely because GV OD and the depletion interaction threshold might not scale linearly. At 5 mg/ml, larger particle sizes were observed for both samples, but these measurements showed large standard deviations. Upon closer inspection of the individual measurements, large fluctuations were seen for the 5 mg/ml sample compared to other samples (Figure A.2b&c). These large fluctuations are likely due to the high viscosity of the sample interfering with the measurements. For future work, more concentrations of alginate need to be taken into account, while staying below 5 mg/ml for a lower viscosity.

Characterizing GV assembly size at various concentrations of alginate using TEM was also unsuccessful. TEM grid preparation of viscous alginate samples proved tedious. Removing excess sample from the TEM grids via wicking was not always possible, resulting in sample layers thicker than 200 µm on the TEM grid that electrons could not penetrate (Figure A.2d). In addition, uranyl acetate staining was not possible, due to the gelating effect that positively charged uranyl ions have on alginate. This made it more difficult to obtain adequate contrast in TEM images. In the future, alternative TEM grid preparation strategies should be explored for higher quality samples. For example, lower OD GV samples could be prepared such that lower concentrations of alginate can be used. However, this will lead to a lower number of GVs in TEM images. Furthermore, a more accurate scaling of GV OD to alginate depletion interaction threshold concentration would need to be found, as these parameters might not scale linearly.

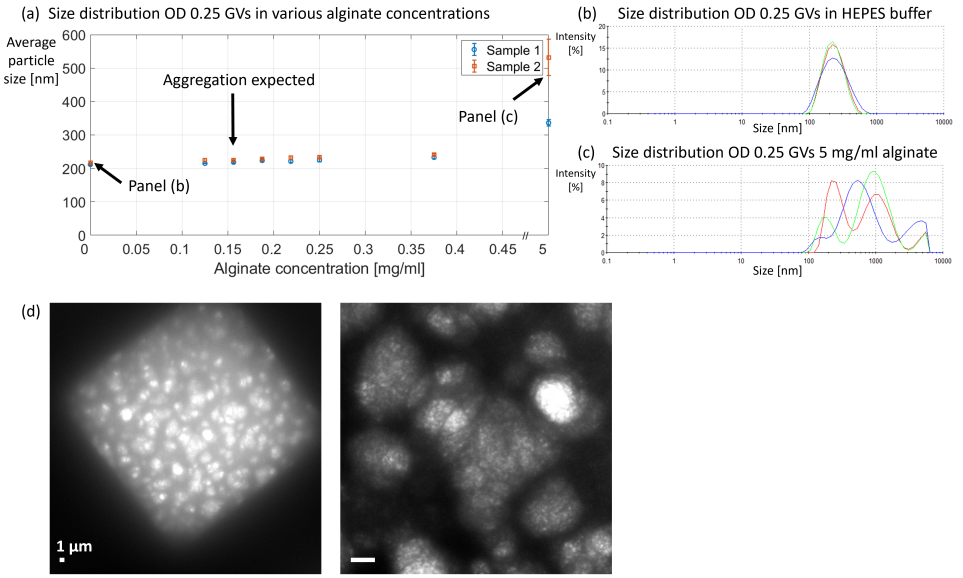

Figure A.2: Inconclusive dynamic light scattering and TEM results. (a) Average size distribution of GVs (OD = 0.25) in various concentrations of alginate. Errorbars represent 1 standard deviation. No aggregation was observed for 2 sets of samples, measured 3 times, at and above the expected concentration, except for 5 mg/ml alginate. However, this showed a large standard deviation. (b) DLS results for the second sample of GVs (OD = 0.25) in HEPES buffer show a size of roughly 244 nm. (c) DLS results for the second sample of GVs (OD = 0.25) in 5 mg/ml show large fluctuations in particle size. Each color in panel (b) and (c) represents individual measurements. (d) TEM images of GVs in 3 mg/ml alginate. A thick viscous layer on the TEM grid prevented electron penetration. Scale bars represent 1 µm.

A.3 ALTERNATIVE ALGINATE BEADS ULTRASOUND IMAGING METHOD

The first iteration of alginate beads were in the order of 400-500 microns because lower flow rates were used during the microfluidic fabrication. The beads were therefore too large for the pipette tips used for filling agarose well phantoms. As an alternative to imaging alginate beads in a well phantom, an imaging approach was implemented where the beads were injected into a large well inside of an agarose slab with a syringe and imaged from the side (see Figure A.3a). This imaging method also removed possible reflections that could be caused by agarose-alginate bead interfaces. The beads were rotating inside the large well to avoid sinking, and the rotation was induced by a 1 mm magnetic stir bar and a magnet plate (Thermofisher Scientific, Waltham, MA, USA) set at 1500 RPM below the agarose slab. Ultrasound images were taken from the side with a layer of ultrasound gel between the transducer and the agarose block, to prevent any air space between the transducer and the agarose. Linear B-mode images were taken at 2 V, while nonlinear xAM images were taken at 15 V (Figure A.3b). In both cases, bright point-source scatterers can be seen in the images of all three beads, while this was only expected for the B-mode images of WT and hGVs and the xAM image of hGVs. These observations could have a combination of three possible explanations. First, all three types of beads possibly have microscopic air-filled cavities, which could be the result of the gelation strategy [66]. In this case, the entrapped air significantly scatters incoming sound waves and appears in ultrasound images as bright pixels. Second, the motion of the stir bar could produce bubbles inside the buffer solution, which in turn could appear as bright point-source scatterers in the ultrasound images. Lastly, the motion of the beads could cause artifacts in imaging modes that require transmitting and receiving many pulses in short succession, such as xAM used here. This is likely the reason that the reflections appear very elongated and smeared. In the future, to avoid the generation of bubbles or motion-based artifacts, the ultrasound imaging of alginate beads could best be done in agarose well phantoms.

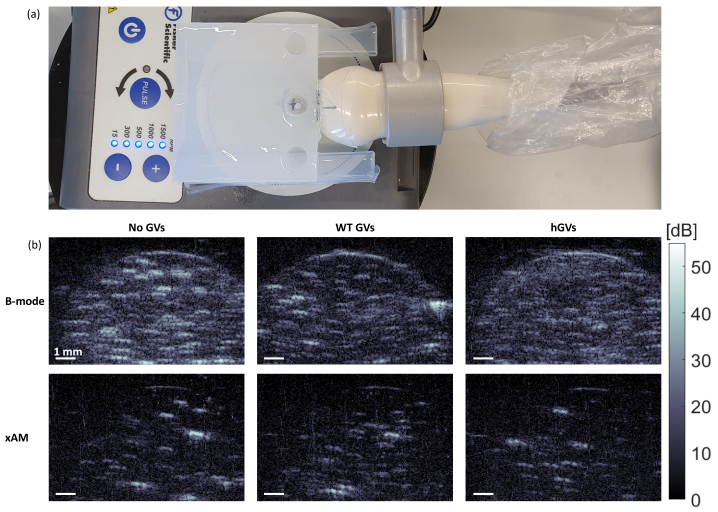

Figure A.3: Ultrasound imaging of moving alginate beads. (a) Ultrasound imaging setup. The probe was placed to the side of an agarose slab with a well into which the alginate bead solution was injected. The well also contained a magnetic stir bar of 1 mm which was rotated using a magnet plate below the agarose. (b) Ultrasound images using linear BMode (top row) and nonlinear xAM (bottom row) of beads without GVs (left column), beads containing WT GVs (middle column) and beads containing hGVs. In all cases, bright point-source scatterers were observed. Scale bars represent 1 mm.

A.4 THE NEXT MICROFLUIDIC CHIP DESIGN

While the microfluidic chip used to create the microscale alginate beads in chapter 2 was capable of producing monodisperse droplets at a fast rate, it could not allow for reliable on-chip alginate gelation and created droplets that were far larger than desired. Therefore, a more complex microfluidic chip was investigated based on the design proposed by Pittermanova et al. [73], since they managed to fabricate beads of several microns through solvent extraction and with on-chip gelation (Figure A.4a). The fabrication of the silicone master and PDMS chip was similar to the simpler flow-focusing chip as described in chapter 2. The microfluidic setup was also similar, but now three syringe pumps were used instead of two. The dispersed phase supplied to the innermost inlet consisted of a 1% alginate solution with either WT or hGVs, or buffer, and had a flow rate of Q_d = 5 µl h^{-1}. The continuous phase supplied to the middle inlet consisted of 1-undecanol (Sigma Aldrich, St. Louis, MO, USA) with 0.1% Picosurf surfactant, and had a flow rate of Q_{c1} = 150 µl h^{-1}. Finally, the second continuous phase, which was supplied to the outermost inlet, was 1-undecanol with 0.1% Picosurf surfactant and 0.5% w/w $CaCl_2$, and had a flow rate of Q_{c2} = 50 µl h^{-1}.

Unfortunately, the small channel dimensions posed a problem. Especially at the successive double T-junctions, where the channel width was 40 µm, dust or small debris could easily get trapped (Figure A.4b). This could also occasionally occur in the simpler microfluidic chip from chapter 2, but there, increasing the flow rate of the continuous and dispersed phases would typically push the debris away. However, increasing the flow rates was not possible for the complex chip, as the pressure in the narrow channels would build up rapidly, causing leakages and making the chip unusable. Taking great care and extensive cleaning steps during the fabrication of the PDMS chip, as well as filtering all solutions before use, could potentially prevent debris from entering the chip. It is also advised to never reinsert microfluidic tubing into the same inlet or outlet, as this could scrape the PDMS and introduce debris into the channels. Nevertheless, unless the chips are made and used in a clean room, debris is difficult to avoid and could always pose a problem when working at such small dimensions.

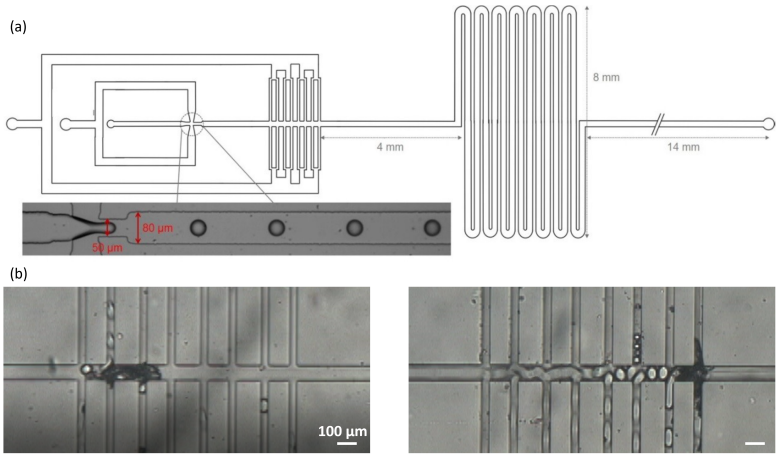

Figure A.4: Complex microfluidic chip design. (a) Microfluidic chip design by Pittermanova et al. that is capable of producing 5 µm alginate beads (from [73]). (b) Two single frame snapshots through an inverted light microscope of the successive T-junctions of the above microfluidic chip design, showing pieces of debris that are stuck in the channels. Scale bars represent 100 µm.

B BIBLIOGRAPHY

[1] R. Hooke, *The Posthumous Works of Robert Hooke Containing His Cutlerian Lectures, and Other Discourses, Read at the Meetings of the Illustrious Royal Society.* S. Smith and B. Walford, 1705.

[2] N. J. Mclellan, "Robert Hooke (1635 – 1703): recognising a sound imagination," *The Lancet*, vol. 352, no. 9124, pp. 312–313, 1998.

[3] T. L. Szabo, *Diagnostic Ultrasound Imaging: Inside out*, 2nd ed. Elsevier Academic Press, 2014.

[4] C. Rabut, S. Yoo, R. C. Hurt, Z. Jin, H. Li, H. Guo, B. Ling, and M. G. Shapiro, "Ultrasound Technologies for Imaging and Modulating Neural Activity," *Neuron*, vol. 108, no. 1, pp. 93–110, 2020.

[5] B. Heiles, D. Terwiel, and D. Maresca, "The Advent of Biomolecular Ultrasound Imaging," *Neuroscience*, pp. 1–12, 2021.

[6] P. Frinking, T. Segers, Y. Luan, and F. Tranquart, "Three Decades of Ultrasound Contrast Agents: A Review of the Past, Present and Future Improvements," *Ultrasound in Medicine and Biology*, vol. 46, no. 4, pp. 892–908, 2020.

[7] M. G. Shapiro, P. W. Goodwill, A. Neogy, M. Yin, F. S. Foster, D. V. Schaffer, and S. M. Conolly, "Biogenic gas nanostructures as ultrasonic molecular reporters," *Nature Nanotechnology*, vol. 9, no. 4, pp. 311–316, 2014.

[8] D. Maresca, T. Payen, A. Lee-Gosselin, B. Ling, D. Malounda, C. Demené, M. Tanter, and M. G. Shapiro, "Acoustic biomolecules enhance hemodynamic functional ultrasound imaging of neural activity," *NeuroImage*, vol. 209, no. November 2019, pp. 0–7, 2020.

[9] A. Lakshmanan, A. Farhadi, S. P. Nety, A. Lee-Gosselin, R. W. Bourdeau, D. Maresca, and M. G. Shapiro, "Molecular Engineering of Acoustic Protein Nanostructures," *ACS Nano*, vol. 10, no. 8, pp. 7314–7322, 2016.

[10] A. Farhadi, G. H. Ho, D. P. Sawyer, R. W. Bourdeau, and M. G. Shapiro, "Ultrasound imaging of gene expression in mammalian cells," *Science*, vol. 365, no. 6460, pp. 1469–1475, 2019.

[11] A. Lakshmanan, Z. Jin, S. P. Nety, D. P. Sawyer, A. Lee-Gosselin, D. Malounda, M. B. Swift, D. Maresca, and M. G. Shapiro, "Acoustic biosensors for ultrasound imaging of enzyme activity," *Nature Chemical Biology*, vol. 16, no. 9, pp. 988–996, 2020.

[12] B. Ling, J. Lee, D. Maresca, A. Lee-Gosselin, D. Malounda, M. B. Swift, and M. G. Shapiro, "Biomolecular Ultrasound Imaging of Phagolysosomal Function," *ACS Nano*, vol. 14, no. 9, pp. 12 210–12 221, 2020.

[13] Q. Huang and Z. Zeng, "A review on real-time 3d ultrasound imaging technology," *BioMed research international*, vol. 2017, 2017.

[14] H. F. Routh, "Doppler ultrasound," *IEEE Engineering in Medicine and Biology Magazine*, vol. 15, no. 6, pp. 31–40, 1996.

[15] H. D. Liang, J. Alison Noble, and P. N. Wells, "Recent advances in biomedical ultrasonic imaging techniques," *Interface Focus*, vol. 1, no. 4, pp. 475–476, 2011.

[16] M. Tanter and M. Fink, "Ultrafast imaging in biomedical ultrasound," *IEEE Transactions on Ultrasonics, Ferroelectrics, and Frequency Control*, vol. 61, no. 1, pp. 102–119, 2014.

[17] H. C. Shin, R. Prager, H. Gomersall, N. Kingsbury, G. Treece, and A. Gee, "Estimation of Average Speed of Sound Using Deconvolution of Medical Ultrasound Data," *Ultrasound in Medicine and Biology*, vol. 36, no. 4, pp. 623–636, 2010.

[18] C. W. Chung, J. S. Popovics, and L. J. Struble, "Using ultrasonic wave reflection to measure solution properties," *Ultrasonics Sonochemistry*, vol. 17, no. 1, pp. 266–272, 2010.

[19] V. Chan and A. Perlas, "Basics of ultrasound imaging," in *Atlas of ultrasound-guided procedures in interventional pain management*. Springer US, 2011, pp. 13–19.

[20] A. P. Yoganathan, E. G. Cape, H.-W. Sung, F. P. Williams, and A. Jimoh, "Review of hydrodynamic principles for the cardiologist: applications to the study of blood flow and jets by imaging techniques," *Journal of the American College of Cardiology*, vol. 12, no. 5, pp. 1344–1353, 1988.

[21] K. K. Shung, *Diagnostic ultrasound: Imaging and blood flow measurements*. CRC press, 2005.

[22] K. H. Taber, K. J. Black, and R. A. Hurley, "Blood flow imaging of the brain: 50 years experience," *The Journal of neuropsychiatry and clinical neurosciences*, vol. 17, no. 4, pp. 441–446, 2005.

[23] K. Miles and R. Williams, "Warburg revisited: imaging tumour blood flow and metabolism," *Cancer Imaging*, vol. 8, no. 1, p. 81, 2008.

[24] Y.-C. Huang, T. L. Ringold, J. S. Nelson, and B. Choi, "Noninvasive blood flow imaging for real-time feedback during laser therapy of port wine stain birthmarks," *Lasers in Surgery and Medicine: The Official Journal of the American Society for Laser Medicine and Surgery*, vol. 40, no. 3, pp. 167–173, 2008.

[25] H. Ramakonar, B. C. Quirk, R. W. Kirk, J. Li, A. Jacques, C. R. Lind, and R. A. McLaughlin, "Intraoperative detection of blood vessels with an imaging needle during neurosurgery in humans," *Science advances*, vol. 4, no. 12, p. eaav4992, 2018.

[26] M. Cikes, L. Tong, G. R. Sutherland, and J. D'Hooge, "Ultrafast cardiac ultrasound imaging: Technical principles, applications, and clinical benefits," *JACC: Cardiovascular Imaging*, vol. 7, no. 8, pp. 812–823, 2014.

[27] H.-X. Xu, "Contrast-enhanced ultrasound: The evolving applications," *World Journal of Radiology*, vol. 1, no. 1, p. 15, 2009.

[28] O. Couture, V. Hingot, B. Heiles, P. Muleki-Seya, and M. Tanter, "Ultrasound Localization Microscopy and Super-Resolution: A State of the Art," *IEEE Transactions on ultrasonics, ferroelectrics and frequency control.*, vol. 65, no. 8, 2018.

[29] C. Demene, J. Robin, A. Dizeux, B. Heiles, M. Pernot, M. Tanter, and F. Perren, "Transcranial ultrafast ultrasound localization microscopy of brain vasculature in patients," *Nature Biomedical engineering*, vol. 5, no. 3, pp. 219–228, 2021.

[30] E. Mace, G. Montaldo, I. Cohen, M. Baulac, M. Fink, and M. Tanter, "Functional ultrasound imaging of the brain," *Nature Methods*, vol. 8, no. 8, pp. 662–664, 2011.

[31] C. Errico, B. F. Osmanski, S. Pezet, O. Couture, Z. Lenkei, and M. Tanter, "Transcranial functional ultrasound imaging of the brain using microbubble-enhanced ultrasensitive Doppler," *NeuroImage*, vol. 124, pp. 752–761, 2016.

[32] S. R. Wilson and P. N. Burns, "Microbubble contrast for radiological imaging," *Ultrasound Quarterly*, vol. 22, no. 1, pp. 15–18, 2006.

[33] M. Overvelde, V. Garbin, J. Sijl, B. Dollet, N. de Jong, D. Lohse, and M. Versluis, "Nonlinear shell behavior of phospholipid-coated microbubbles," *Ultrasound in Medicine and Biology*, vol. 36, no. 12, pp. 2080–2092, 2010.

[34] J. E. Chômas, P. Dayton, J. Alien, K. Morgan, and K. W. Ferrara, "Mechanisms of contrast agent destruction," *IEEE Transactions on Ultrasonics, Ferroelectrics, and Frequency Control*, vol. 48, no. 1, pp. 232–248, 2001.

[35] A. E. Walsby, "Gas vesicles," *Microbiological Reviews*, vol. 58, no. 1, pp. 94–144, 1994.

[36] A. Lakshmanan, G. J. Lu, A. Farhadi, S. P. Nety, M. Kunth, A. Lee-Gosselin, D. Maresca, R. W. Bourdeau, M. Yin, J. Yan, C. Witte, D. Malounda, F. S. Foster, L. Schröder, and M. G. Shapiro, "Preparation of biogenic gas vesicle nanostructures for use as contrast agents for ultrasound and MRI," *Nature Protocols*, vol. 12, no. 10, pp. 2050–2080, 2017.

[37] R. C. Hurt, M. T. Buss, K. Wong, D. P. Sawyer, M. B. Swift, P. Dutka, D. R. Mittelstein, Z. Jin, M. H. Abedi, R. Deshpande, and M. G. Shapiro, "Genomically Mined Acoustic Reporter Genes Enable On-Demand In Vivo Monitoring of Tumor-Homing Bacteria 1," *bioRxiv preprint*, 2021.

[38] S. T. Huber, D. Terwiel, W. H. Evers, D. Maresca, and A. J. Jakobi, "Cryo-EM Structure of Gas Vesicles for Buoyancy-Controlled Motility," *bioRxiv preprint*, 2022.

[39] D. Maresca, A. Lakshmanan, A. Lee-Gosselin, J. M. Melis, Y. L. Ni, R. W. Bourdeau, D. M. Kochmann, and M. G. Shapiro, "Nonlinear ultrasound imaging of nanoscale acoustic biomolecules," *Applied Physics Letters*, vol. 110, no. 7, pp. 1–5, 2017.

[40] D. Maresca, D. P. Sawyer, G. Renaud, A. Lee-Gosselin, and M. G. Shapiro, "Nonlinear X-Wave Ultrasound Imaging of Acoustic Biomolecules," *Physical Review X*, vol. 8, no. 4, pp. 1–12, 2018.

[41] V. Perrot, M. Polichetti, F. Varray, and D. Garcia, "So you think you can DAS? A viewpoint on delay-and-sum beamforming," *Ultrasonics*, vol. 111, pp. 1–12, 2021.

[42] D. Maresca, A. Lakshmanan, M. H. Abedi, A. Bar-Zion, A. Farhadi, G. J. Lu, J. O. Szablowski, D. Wu, S. Yoo, and M. G. Shapiro, "Biomolecular Ultrasound and Sonogenetics," *Annu Rev Chem Biomol Eng*, vol. 9, pp. 229–252, 2018.

[43] M.-X. Tang and R. J. Eckersley, "Frequency and pressure dependent attenuation and scattering by microbubbles," *Ultrasound in medicine & biology*, vol. 33, no. 1, pp. 164–168, 2007.

[44] M. Emmer, H. J. Vos, D. E. Goertz, A. van Wamel, M. Versluis, and N. de Jong, "Pressure-dependent attenuation and scattering of phospholipid-coated microbubbles at low acoustic pressures," *Ultrasound in medicine & biology*, vol. 35, no. 1, pp. 102–111, 2009.

[45] L. Chinchilla, C. Armstrong, R. Mehri, A. S. Savoia, M. Fenech, and E. Franceschini, "Numerical investigations of anisotropic structures of red blood cell aggregates on ultrasonic backscattering," *The Journal of the Acoustical Society of America*, vol. 149, no. 4, pp. 2415–2425, 2021.

[46] V. Leroy, A. Bretagne, M. Fink, H. Willaime, P. Tabeling, and A. Tourin, "Design and characterization of bubble phononic crystals," *Applied Physics Letters*, vol. 95, no. 17, pp. 1–4, 2009.

[47] A. Bretagne, A. Tourin, and V. Leroy, "Enhanced and reduced transmission of acoustic waves with bubble meta-screens," *Applied Physics Letters*, vol. 99, no. 22, pp. 5–7, 2011.

[48] P. A. Deymier, *Acoustic metamaterials and phononic crystals*. Springer Heidelberg, 2013.

[49] Y. Yao, Z. Jin, B. Ling, D. Malounda, and M. G. Shapiro, "Self-assembly of protein superstructures by physical interactions under cytoplasm-like conditions," *Biophysical Journal*, vol. 120, no. 13, pp. 2701–2709, 2021.

[50] W. Li and H. R. Ma, "Depletion interactions between two spherocylinders," *Eur. Phys. J. E*, vol. 16, pp. 225–231, 2005.

[51] A. V. Petukhov, R. Tuinier, and G. J. Vroege, "Entropic patchiness: Effects of colloid shape and depletion," *Current Opinion in Colloid and Interface Science*, vol. 30, pp. 54–61, 2017.

[52] T. Hu and A. C. Lo, "Collagen–alginate composite hydrogel: Application in tissue engineering and biomedical sciences," *Polymers*, vol. 13, no. 11, 2021.

[53] K. Y. Lee and D. J. Mooney, "Alginate: Properties and biomedical applications," *Progress in Polymer Science (Oxford)*, vol. 37, no. 1, pp. 106–126, 2012.

[54] C. Bondy, "The creaming of rubber latex," *Transactions of the Faraday Society*, vol. 35, pp. 1093–1108, 1939.

[55] A. Moreira, J. Carneiro, J. B. Campos, and J. M. Miranda, "Production of hydrogel microparticles in microfluidic devices: a review," *Microfluidics and Nanofluidics*, vol. 25, no. 2, pp. 1–24, 2021.

[56] G. M. Whitesides, "The origins and the future of microfluidics," *Nature*, vol. 442, no. July, pp. 368–373, 2006.

[57] X. J. Li, Y. Zhou, X. J. Li, and Y. Zhou, *Microfluidic Devices for Biomedical Applications*. Jordon Hill, United Kingdom: Elsevier Science & Technology, 2013.

[58] S. Y. Park, T. H. Wu, Y. Chen, M. A. Teitell, and P. Y. Chiou, "High-speed droplet generation on demand driven by pulse laser-induced cavitation," *Lab on a Chip*, vol. 11, no. 6, pp. 1010–1012, mar 2011.

[59] S.-Y. Teh, R. Lin, L.-H. Hung, and A. P. Lee, "Droplet microfluidics," *Lab on a Chip*, vol. 8, no. 2, pp. 198–220, 2008.

[60] R. Seemann, M. Brinkmann, T. Pfohl, and S. Herminghaus, "Droplet based microfluidics," *Reports on Progress in Physics*, vol. 75, no. 1, 2012.

[61] G. F. Christopher and S. L. Anna, "Microfluidic methods for generating continuous droplet streams," *Journal of Physics D: Applied Physics*, vol. 40, no. 19, 2007.

[62] G. B. Kim, Y. R. Park, S. J. Kim, and K. H. Park, "Effect of Intersection Angle of Input Channels in Droplet Generators," *Molecules*, vol. 27, no. 6, 2022.

[63] M. Y. A. Jamalabadi, M. DaqiqShirazi, A. Kosar, and M. S. Shadloo, "Effect of injection angle, density ratio, and viscosity on droplet formation in a microfluidic t-junction," *Theoretical and Applied Mechanics Letters*, vol. 7, no. 4, pp. 243–251, 2017.

[64] A. M. Ibrahim, J. I. Padovani, R. T. Howe, and Y. H. Anis, "Modeling of droplet generation in a microfluidic flow-focusing junction for droplet size control," *Micromachines*, vol. 12, no. 6, pp. 1–11, 2021.

[65] J K Nunes, S. S. H. Tsai1, J. Wan, and H. A. Stone1, "Dripping and jetting in microfluidic multiphase flows applied to particle and fiber synthesis," *Cancer Research*, vol. 10, no. 12, pp. 5014–5023, 2010.

[66] F. Stops, J. T. Fell, J. H. Collett, and L. G. Martini, "Floating dosage forms to prolong gastro-retention—the characterisation of calcium alginate beads," *International journal of pharmaceutics*, vol. 350, no. 1-2, pp. 301–311, 2008.

[67] C. Burch and J. Stock, "Phase-contrast microscopy," *Journal of Scientific Instruments*, vol. 19, no. 5, p. 71, 1942.

[68] Y. Hu, Q. Wang, J. Wang, J. Zhu, H. Wang, and Y. Yang, "Shape controllable microgel particles prepared by microfluidic combining external ionic crosslinking," *Biomicrofluidics*, vol. 6, no. 2, pp. 1–9, 2012.

[69] A. Farhadi, M. Bedrossian, J. Lee, G. H. Ho, M. G. Shapiro, and J. L. Nadeau, "Genetically Encoded Phase Contrast Agents for Digital Holographic Microscopy," *Nano Letters*, 2020.

[70] A. Bar-Zion, A. Nourmahnad, D. R. Mittelstein, S. Shivaei, S. Yoo, M. T. Buss, R. C. Hurt, D. Malounda, M. H. Abedi, A. Lee-Gosselin *et al.*, "Acoustically triggered mechanotherapy using genetically encoded gas vesicles," *Nature Nanotechnology*, vol. 16, no. 12, pp. 1403–1412, 2021.

[71] E. Rondeau and J. J. Cooper-White, "Biopolymer microparticle and nanoparticle formation within a microfluidic device," *Langmuir*, vol. 24, no. 13, pp. 6937–6945, 2008.

[72] S. Sugaya, M. Yamada, A. Hori, and M. Seki, "Microfluidic production of single micrometer-sized hydrogel beads utilizing droplet dissolution in a polar solvent," *Biomicrofluidics*, vol. 7, no. 5, 2013.

[73] A. Pittermannová, Z. Ruberová, A. Zadražil, N. Bremond, J. Bibette, and F. Štěpánek, "Microfluidic fabrication of composite hydrogel microparticles in the size range of blood cells," *RSC Advances*, vol. 6, no. 105, pp. 103 532–103 540, 2016.

[74] T. Heinze, T. Liebert, B. Heublein, and S. Hornig, "Functional polymers based on dextran," *Advances in Polymer Science*, vol. 205, no. 1, pp. 199–291, 2006.

[75] B. J. Berne and R. Pecora, *Dynamic light scattering: with applications to chemistry, biology, and physics*. Courier Corporation, 2000.

TU Delft

Erasmus MC
University Medical Center Rotterdam